Understanding the fate of H_2S injected in basalts by means of time-domain induced polarization geophysical logging

L. Lévy[1,2], Daniel A. Ciraula[3], Bruno Legros[4], T. Martin[1], A. Weller[5]

[1]Engineering Geology, Lund University, Lund, Sweden
[2]ÍSOR - Iceland GeoSurvey, Kópavogur, Iceland
[3]Nordic Volcanological Center, Institute of Earth Sciences, University of Iceland, Reykjavík, Iceland
[4]Advanced Logic Technology, Luxembourg
[5]Institut für Geologie und Paläontologie, Technische Universität Clausthal, Germany

Key Points:

- H_2S reinjection in basalt and mineralization into pyrite was monitored using TDIP logging in two of the injection wells
- Chargeability increases observed at +40 days (first monitoring round) correspond to 1-2% pyrite precipitation with great spatial variability
- Subsequent monitoring rounds show a decrease in chargeability, suggesting that pyrite is either passivated or re-dissolved

Corresponding author: Léa Lévy, `lea.levy@tg.lth.se`

Abstract

To help meet emission standards, hydrogen sulfide (H_2S) from geothermal production may be injected back into the subsurface, where basalt offers, in theory, the capacity to mineralize H_2S into pyrite. Ensuring the viability of this pollution mitigation technology requires information on how much H_2S is mineralized, at what rate and where. To date, monitoring efforts of field-scale H_2S reinjection have mostly occurred via mass balance calculations, typically capturing less than 5% of the injected fluid. While these studies, along with laboratory experiments and geochemical models, conclude effective H_2S mineralization, their extrapolation to quantify mineralization and its persistence over time leads to considerable uncertainty. Here, a geophysical methodology, using time-domain induced polarization (TDIP) logging in two of the injection wells (NN3 and NN4), is developed to follow the fate of H_2S re-injected at Nesjavellir geothermal site in south-west Iceland. Results show a strong chargeability increase at +40 days, corresponding to precipitation of up to 1% in NN4 and 2% in NN3 according to laboratory-based relationships. A uniform increase is observed along NN4, whereas it is localized below 450 in NN3. Changes are more pronounced with the larger electrode spacing, indicating that pyrite precipitation takes place away from the wells. Furthermore, a chargeability decrease is observed at later monitoring rounds in both wells, suggesting that pyrite is either passivated or re-dissolved after precipitating. These results highlight the ability of TDIP logging to monitor pyrite mineralization and have implications for understanding the fate of H_2S upon subsurface storage in basaltic environments.

Plain Language Summary

High-temperature geothermal production is responsible for air pollution due to hydrogen sulfide (H_2S) present in the magmatic fluid. To help meet emission standards, H_2S may be injected back into the subsurface, where basalt offers the capacity to transform H_2S into pyrite. Transformation into an immobile mineral prevents further transport into the atmosphere, sea, surface streams, or lakes. However, ensuring the viability of this pollution mitigation technology requires information such as how much H_2S is mineralized, at what rate and where, which are highly uncertain due to the heterogeneity and inaccessibility of subsurface processes. Here, a geophysical monitoring methodology is developed and tested during the re-injection of H_2S at Nesjavellir geothermal site in south-west Iceland. According to laboratory studies, pyrite precipitation is expected to increase the electrical capacitance, "chargeability", of the subsurface. Using the so-called time-domain induced-polarization (TDIP) method embedded in a wireline logging tool, the chargeability of a 2m-wide cylinder around the injection wells is measured with high spatial-resolution before and during H_2S injection. A strong chargeability increase at +40 days indicates that up to 2% pyrite is formed. A subsequent decrease at later rounds raises questions on whether pyrite is re-dissolved or passivated by other secondary minerals.

1 Introduction

Geothermal energy production emits an estimated 0.2 Mt/yr of hydrogen sulfide (H_2S) globally, with Iceland alone emitting 30kt/yr (Marieni et al., 2018). These anthropogenic H_2S emissions are sourced from the geothermal production steams, which contain significant concentrations of H_2S (Prikryl et al., 2018; Stefánsson et al., 2011). H_2S emissions are toxic to humans and can be fatal in concentrations as low as 320 ppm (World Health Organization - Regional Office for Europe, 2000). H_2S emissions also pose a threat to the environment, oxidizing when exposed to atmospheric oxygen to form acid rain (Greaver et al., 2012). Recent air quality regulations, both internationally and within Iceland, have limited the amount of H_2S atmospheric emissions to 50-150 µg/m3 per 24 hours (Aradóttir

et al., 2015; World Health Organization - Regional Office for Europe, 2000; Iceland Ministry of the Environment, Energy and Climate, 2010).

To reduce emissions from geothermal energy production in Iceland, H_2S can be dissolved into the geothermal wastewater and injected into the basalt subsurface (Mamrosh et al., 2014). To help meet emission standards, H_2S from the geothermal production steam may be captured at the power plant, dissolved into geothermal wastewater, and injected into the basalt subsurface (Mamrosh et al., 2014). Geochemical and reactive transport models suggest that such a H_2S-injection results in effective sulfide mineralization, with pyrite being the dominant sulfur bearing mineral (Prikryl et al., 2018; Stefánsson et al., 2011; Marieni et al., 2018; Bacon et al., 2014), due to the high reactivity of basalt and its divalent cations content (up to 25 wt.% Ca, Mg, Fe) (Matter et al., 2016; Gysi & Stefánsson, 2008). However, these findings are based on simulations and laboratory experiments with limited evidence from field tests (Robin et al., 2020). In practice, the H_2S mineral storage process requires careful monitoring to identify any adverse effects of the injection, such as the acidification of the shallow groundwater system and the mobilization of toxic metals from the basaltic rocks (Floor et al., 2011; Cuoco et al., 2013; Delmelle et al., 2015; Galeczka et al., 2016; Flaathen & Gislason, 2007).

Current monitoring practices for H_2S mineralization into pyrite are similar to those for CO_2 mineralization into carbonates. They consist mainly of quantification by (i) mass balance calculations using tracer tests (Matter et al., 2016), (ii) transport models (Ratouis et al., 2022), and (iii) steady-state "reaction path" geochemical models based on chemical monitoring. Chemical and mineral analyses on precipitates formed on metallic surfaces within monitoring wells also bring qualitative mineralization evidence (Matter et al., 2016). More recently, the triple sulfur isotope systematics (32S, 33S, and 34S) of geothermal fluids were investigated as a possible tool to trace H_2S sequestration by sulfide mineralization in the geothermal reservoir (Robin et al., 2020). One major pitfall of these monitoring practices is that they typically capture less than 5% of the flow and extrapolate the results (Matter et al., 2016), whereas the remaining 95% may include undetected upward migration through fractures and springs. In addition, a key assumption behind the quantification is that the amount of dissolved gas not captured by the measurement downstream, compared to expectations, has mineralized and that mineralization is permanent (Gunnarsson et al., 2018; Matter et al., 2016). While physical verification of these assumptions, e.g., through post-injection core-drilling, has not yet been possible (Carbfix, 2022), other studies focusing on CO_2 indicate that additional processes to carbonate mineralization can happen, namely the formation of unstable organic carbon due to microbial activity (Trias et al., 2017). Therefore, quantifying mineralization with these methods, whether sulfide or carbonate, leads to considerable uncertainty (White et al., 2020).

Time-lapse geophysics is a group of potentially suitable methods to obtain in-situ information on the spatial distribution and magnitude of H_2S mineralization, as well as its evolution over time. Time-lapse geophysics as a monitoring technique can, in theory, capture dynamic processes with high spatial and temporal resolutions (Hermans et al., 2023; Lévy et al., 2022). Geo-electrical methods are particularly suitable for pyrite detection. Underground massive metallic ore deposits, as well as veinlets and disseminated sulfides, have been detected and discriminated with induced polarization (IP) field measurements (Pelton et al., 1978; Placencia-Gómez, 2015; Börner et al., 2018). Petrophysical laboratory measurements also indicate that the presence of pyrite can be detected in altered volcanic rocks and quantified to some extent, with induced polarization (Lévy, Gibert, et al., 2019). The polarizability, also called chargeability, describes the amplitude of electrical polarization in rocks, which is particularly strong at interfaces between fluid and semi-conductors, such as pyrite or magnetite (Bücker et al., 2018; Gurin et al., 2015; Abdulsamad et al., 2017). The reorganization of charges at the interface between pore fluid and metallic particles creates local electrical "displacement" currents, which add up until a maximum voltage is reached. The time-delay between maximum voltage

and maximum current, also known as the phase-angle for sinusoidal signals, is caused by the polarization (Bücker et al., 2018; Chelidze & Gueguen, 1999; Olhoeft, 1985). On the other hand, the conductivity quantifies the amplitude of the electric conduction phenomenon in rocks, which is in particular enhanced by the presence of smectite, as well as high porosity, salinity, and temperature (Flóvenz et al., 2005; Kristinsdóttir et al., 2010; Lévy et al., 2018; Waxman & Smits, 1968). Geo-electrical field investigations carried out at a geothermal site in North-East Iceland confirmed that the conductivity and IP signals of naturally present pyrite, smectite, and magnetite can be picked up down to 200 m depth (Lévy, Maurya, et al., 2019).

In January 2021, the geothermal power company *ON Power* started a small-scale injection of H_2S and CO_2 dissolved in seal water from liquid-ring vacuum pumps at Nesjavellir, South-West Iceland. This small-scale injection runs alongside larger-scale injection of separated geothermal fluid from the power plant that has been part of standard operations since 1990, shortly after the power plant was installed. The injection takes place in eight shallow wells ranging from 311 m to 660 m deep. We use this injection experiment to investigate the subsurface induced polarization response over time and assess (i) the sensitivity of time-lapse geophysics to pyrite precipitation and (ii) the sustainability of pyrite mineralization. As surface geophysical measurements lose resolution with depth, wireline logging was considered a relevant intermediate scale between laboratory and surface geophysical measurements to assess pyrite precipitation in the vicinity of the injection wells. It is thus the focus of this study.

2 Theory and Background

2.1 Electrical response of pyrite with frequency-domain IP (FDIP)

In an electrical context, geological formations can be thought of as a combination of resistors and capacitors (Lévy, 2019). Ions in pore water and those connected to clay minerals are charge carriers in aquifers. Conductive water and clay minerals can be represented by conductors with high conductivity, as opposed to freshwater and pure quartz sand or gravel, which have lower conductivity. Semi-conducting metallic particles (e.g., pyrite or magnetite) can cause electronic conduction beyond 20% per volume if the particles are interconnected (e.g., veinlets) (Slater et al., 2005, 2006; Revil, Abdel Aal, et al., 2015), but disseminated particles mainly cause electrical polarization, an effect similar to that of a capacitor in an electric circuit. Polarization caused by semi-conductors is usually several orders of magnitude stronger than sediment/water interfaces (Revil et al., 2017; Slater et al., 2005, 2006). This is due to the specifics of the crystal structure of semi-conducting minerals, such as pyrite and magnetite, and the possibility for electrons and holes to "jump" and rapidly redistribute within the metallic particle in response to the external field (Shuey, 2012; Pridmore & Shuey, 1976). This redistribution causes the accumulation of ions at the interface between fluid and metallic particles.

Figure 1 illustrates the large polarization, represented by the phase angle parameter, of volcanic samples containing pyrite, as opposed to a volcanic sample of similar geology and full of smectite but without pyrite; the latter being more conductive but much less polarizable, as described in details by Lévy, Gibert, et al. (2019) and Lévy, Weller, and Gibert (2019). It is also visible in Figure 1 that the grain size distribution of metallic particles affects the frequency at which the phase angle peak occurs.

Several models have been developed to describe how ions reversibly accumulate at the interface between pore fluid and metallic particles, causing polarization. One of the most widespread phenomenological relaxation models to interpret FDIP data is the Pelton model (Pelton et al., 1978; Tarasov & Titov, 2013; Weller & Slater, 2022), given by equation 1.

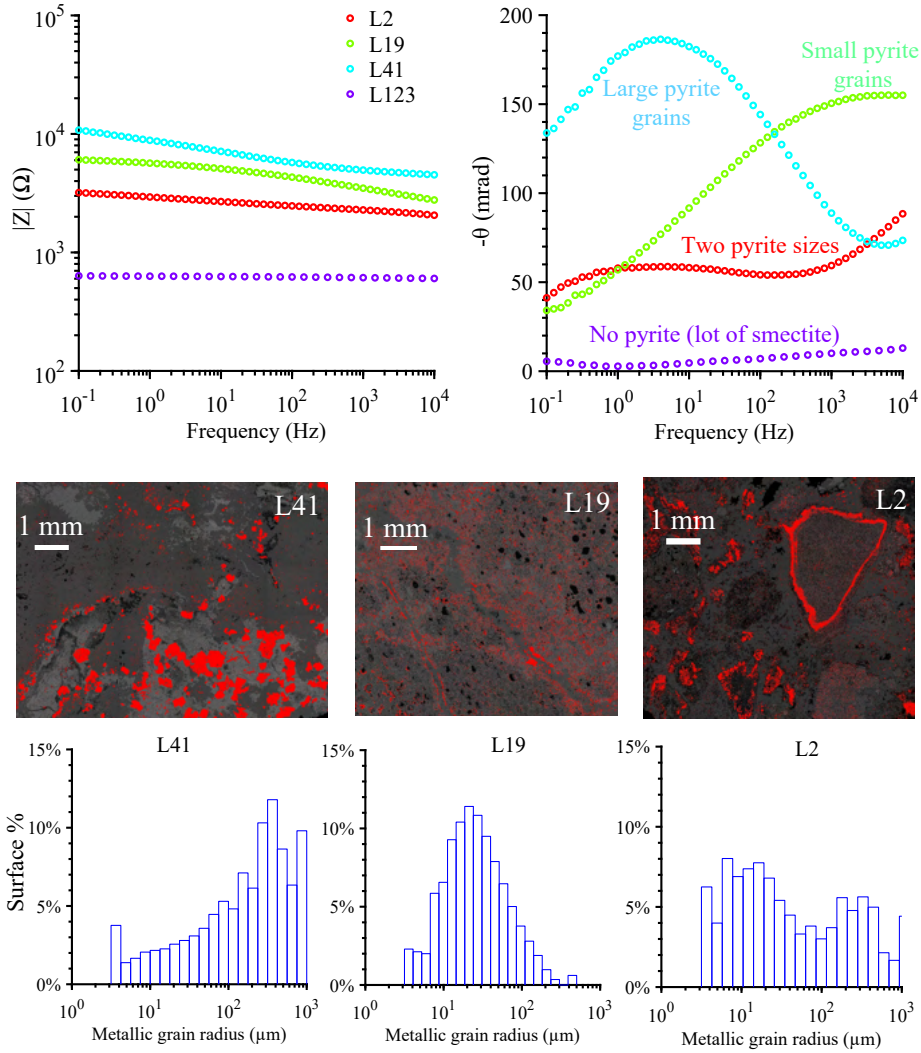

Figure 1. Laboratory results for naturally altered volcanic samples from the Krafla geothermal field (north-east Iceland) containing varying amounts of pyrite with different grain sizes. Top panels: FDIP data for four different samples, left = impedance modulus, right = phase angle, as a function of frequency. Middle panels: scanning electron microscope (SEM) images for the three samples containing pyrite. Pyrite grains are highlighted in red. Bottom panels: distribution of pyrite grain size, based on the SEM images of the three samples.

$$\rho^*(f) = \rho_{DC}[1 - m(1 - \frac{1}{1 + (i2\pi f\tau)^c})] \quad (1)$$

with four fitting parameters: the DC resistivity ρ_{DC}, the chargeability m, the Pelton time constant τ and the so-called Cole–Cole exponent c.

However, the Pelton model, presented in equation 1, is only valid for spectra measured on samples with a single grain size fraction. Variations of this model for two grain size fractions exist but the fitting parameters are not directly comparable to each other, and even the two grain size fractions model may not represent the complexity of naturally occurring pyrite crystals in volcanic rocks (Lévy, Gibert, et al., 2019).

A more general approach to analyzing FDIP data is the Debye decomposition (Nordsiek & Weller, 2008). With this approach, the frequency-dependent complex electrical resistivity $\rho^*(f)$ describes an IP spectrum that can be fitted by a superposition of N Debye terms (Pelton models with $c = 1$), as shown in equation 2.

$$\rho^*(f) = \rho_{DC}[1 - \sum_{k=1}^{N} m_k(1 - \frac{1}{1 + i2\pi f\tau_k})] \quad (2)$$

where m_k and τ_k are pairs of partial chargeability and relaxation time of a single Debye model. The function $m_k = f(\tau_k)$ is also referred to as relaxation time distribution (RTD). The N chargeability values m_k, which are related to a set of pre-defined relaxation times τ_k, and the value of DC resistivity ρ_{DC} are the result of a fitting procedure described by Nordsiek and Weller (2008). Two parameters can be integrated from the Debye decomposition to simplify the interpretations: the total chargeability m_{tot} (equation 3) and the mean relaxation time and τ_{mean} (equation 4).

$$m_{tot} = \sum_{k=1}^{N} m_k \quad (3)$$

$$\tau_{mean} = exp(\frac{\sum_{k=1}^{N} m_k ln(\tau_k)}{m_{tot}}) \quad (4)$$

The main empirical petrophysical relationship linking the chargeability to pyrite volume in the absence of background polarization was developed by Revil, Florsch, and Mao (2015) (equation 5).

$$m = \frac{9}{2} p_v \quad (5)$$

where p_v is the volume fraction of pyrite (or other metallic particles) and m is the chargeability in V/V (dimensionless). In their study, the chargeability parameter is fitted to frequency-domain IP (FDIP) data by a Pelton model (Cole & Cole, 1941; Pelton et al., 1978). According to Martin and Weller (2023), the chargeability m fitted by a Pelton model (Pelton et al., 1978) and m_{tot} fitted by Debye decomposition (Nordsiek & Weller, 2008) are similar for sand-pyrite mixtures.

While the influence of temperature on the polarization effect is still poorly understood, recent laboratory experiments indicate that the phase angle in the presence of metallic particles is temperature independent in the range 5-50°C (Revil et al., 2018).

2.2 Frequency-domain and time-domain induced polarization (FDIP and TDIP)

In the field, the Time Domain Induced Polarization (TDIP) method is often preferred to FDIP, primarily due to its easier and faster implementation. TDIP consists of injecting a direct current pulse of finite duration (DC) through two current electrodes (A and B) and recording the resulting voltage at two potential electrodes (M and N) with a fine-enough sampling rate to capture the exponential charge and discharge of the voltage, during the on-time and off-time, respectively (Sumner, 1976; Telford et al., 1990). Further details on the TDIP methods can be found in Binley and Slater (2020).

In general, voltage discharge measured by TDIP is expected to have a stretched shape, which describes the relaxation behavior in a similar manner as Cole-Cole and other related FDIP models (Alvarez et al., 1991; Cole & Cole, 1941; Davidson & Cole, 1951; Havriliak & Negami, 1966). More details are described in Appendix Appendix A. While quantitatively connecting the TDIP and FDIP responses of rocks containing metallic particles is not trivial (Alvarez et al., 1991), the Debye decomposition is a common method for analyzing both TDIP and FDIP data (Nordsiek & Weller, 2008; Tarasov & Titov, 2007). An equivalence was found by Martin et al. (2021) between the Debye decomposition of FDIP and TDIP data, provided that the current injection time in TDIP was long enough (ideally 64 seconds, but decent comparisons were found beyond 2 seconds). With 2-second current injection, as is the case in this study, the coefficients from the Debye decomposition of TDIP data are slightly underestimated compared to FDIP data. Despite this limit, this approach was considered the most relevant one. As opposed to the integral chargeability, which tends to smoothen out noise in the data, the Debye decomposition tends to amplify the noise and, thus, requires careful data processing (Martin et al., 2021).

3 Materials and Methods

3.1 H_2S production and re-injection at Nesjavellir geothermal field, Iceland

The methodology developed in this study for monitoring H_2S injection was tested at the Nesjavellir geothermal field (SW Iceland), where a geothermal power station has been operated since 1990 (Figure 2). Nesjavellir is a high-temperature geothermal field ($> 200°C$ above 1 km depth) characterized by a relatively high permeability (Zakharova & Spichak, 2012). Nesjavellir is located just north of the Hengill central volcano, which is situated on a ridge-ridge-transform triple junction (Foulger, 1988). The area is comprised of mainly late Quaternary hyaloclastites and post-glacial age hyaloclastites and basalt flows (Árnason et al., 1969; Foulger & Toomey, 1989). This study focuses on shallow depths northeast of the geothermal production area and above the low-permeability clay cap layer (approximately 500 m depth) (Schiffman & Fridleifsson, 1991; Gómez-Díaz et al., 2022; Gunnarsdottir et al., 2020; Franzson & Gunnlaugsson, 2020). Intrusions are rare at these shallow depths, and none have been identified in the upper 300 m (Franzson, 1988).

The Nesjavellir power station currently produces 120 MWe of electricity and 300 MWth of thermal energy for district heating. The hydrothermal production fluid (260-300°C) is sourced at 1000-1500 m depth (Snæbjörnsdóttir et al., 2020). Following a controlled pressure-decrease, the hydrothermal fluid is divided into (i) steam and (ii) geothermal separated water at 192°C. Electricity generation at Nesjavellir uses 240 kg/s of steam to power four turbines. The steam is then condensed, using 2,000 l/s of cold groundwater (5-7°C), to form condensate wastewater, composed primarily of distilled water. In parallel, heat exchangers use the $192°C$ geothermal separated water to heat cold groundwater to 87°C, which is then pumped to the capital Reykjavík, 27 km away. The sep-

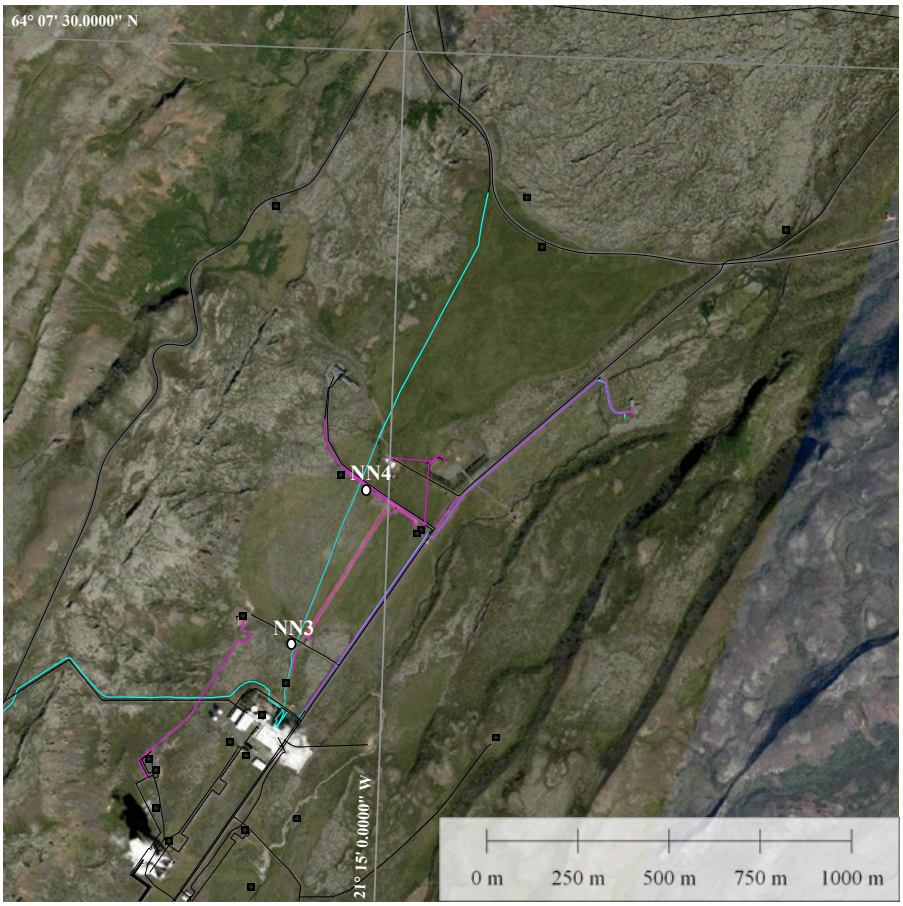

Figure 2. Aerial view of Nesjavellir valley (south-west Iceland). The white building shows the geothermal power plant. The two wells, NN3 and NN4, investigated in this study are indicated by white circles, while other wells in the area are shown with small black rectangle signs. A buried power line (132 kV), most likely responsible for the 50 Hz background noise, is shown in blue. Pipelines are shown in pink and roads in black.

Table 1. Details on the Nesjavellir NN injection wells in this study. The borehole fluid conductivity was measured with a QL40-FTC logging probe (*Mount Sopris QL40-FTC*, 2014) in July 2022 (+540 days). Temperature and caliper logs are presented in Figures B1 and B2 in Appendix Appendix A.

Well ID	NN-3	NN-4
Coordinates	64°06'38.23" N, 21°15'20.27" W	64°06'50.03" N, 21°15'0.06" W
Depth (m)	563	422
Deviation	0°	0°
Casing Depth (m)	205	201
Borehole mean diameter (mm)	405 (min=317 - max=680)	403 (min=324 - max=636)
Average flow Rate (kg/s)	11	113
Injected fluid temperature (°C)	65	85
Borehole temperature while measuring (°C)	63-69	57-71
Reservoir temperature (°C)	15-20	20-40
Borehole fluid conductivity (mS/m)	60-100	100
pH	8.5	9.1
H_2S (ppm)	74.42	76.81
CO_2 (ppm)	13.5	8.35
SiO_2 (ppm)	435.08	428.09

arated water contains the dissolved solids from the hydrothermal fluid and thus has a high potential for chemical pollution and corrosion. Starting in 2004 and prior to 2021, wastewater composed of condensate and separation water has been disposed of in drainage wells. This initial wastewater had negligible concentrations of dissolved CO_2 and H_2S. Starting on January 29th, 2021, a third type of fluid, called seal water, is now mixed into the condensate and separation water before injection. Seal water contains the non-condensable fraction of gases, primarily H_2S, that pose corrosion problems to turbines over time. It is formed by dissolving the CO_2 and H_2S gases from liquid ring vacuum pumps at the condensers in cold groundwater or condensate water. The currently injected wastewater contains, on average, 75 ppm of H_2S (Table 1), with the intention to sequester H_2S through mineral storage.

Two injection wells are used for monitoring: NN3 and NN4, drilled into fresh lavas to 563 m (NN3) and 422 m (NN4) depth in 2001, northeast of the power station. Their specific lithology and alteration stage at the time of drilling (i.e., prior to large-scale warm wastewater injection) are presented in Helgadóttir (2021), emphasizing an increase in the amount of clay minerals below 400 m in NN3. Between 2004 and 2021, injection of the initial wastewater into the cold groundwater system took place through these wells and has probably been enhancing basaltic rock alteration compared to natural conditions. Starting from January 2021, H_2S has been continuously injected through the final wastewater. Reaction path modeling from the literature predicts that basaltic glass dissolution is the main source of iron over short time durations, with magnetite dissolution contributing less iron due to the slower dissolution kinetics and more limited amount. Pyrite precipitation is expected to be rapid (Prikryl et al., 2018; Stefánsson et al., 2011). An overview of the area, including roads, boreholes, and buried infrastructure, is presented in Figure 2. Information on the wells and the injection are given in Table 1. Temperature logs in NN3 and NN4 measured the days of TDIP logging are presented in Figures B1 in Appendix Appendix B, together with caliper logs measured after drilling (Figure B2). Further details on the wells can be found in Gómez-Díaz et al. (2022) and Hafstað (2003).

3.2 Field monitoring with QL40-IP logging tool

The QL40-ELOG/IP (*Mount Sopris QL40-IP*, 2020) logging tool measures the electrical resistivity and time-domain IP (TDIP) response with electrodes made of stainless steel. The tool has a diameter of 43 mm and uses the "normal" electrode configuration with 16- and 64" electrode spacings, defined as the distance between the current electrode (A) and the potential electrode (N) (Helander, 1983). The current generator, built into the tool, sends current at electrode A in all directions and the shielding of the logging wireline serves as the current sink. The reference potential electrode (M) is located on top of an 8m-long isolation bridle, such that the distance between the potential electrodes (M and N) is considered infinite in comparison to the much smaller electrode spacing AN. Moreover, grounding of the logging unit (truck) is achieved by clamping the truck ground onto the casing for security reasons (Advanced Logic Technology, 2021). The 64" measurements are sensitive to polarization effects over a larger measurement volume, deeper into the formation, compared to the 16". The radial investigation characteristic, as defined by Roy and Dhar (1971), considers electrostatic potentials of individual cylindrical shells of varying radii integrated to obtain the total contribution to the measured signal. According to the formula by Roy and Dhar (1971), 75% of the measured signal with the 64" spacing is caused by the cylindrical volume comprised in a 2.5-m radius from the borehole central line. As a comparison, 75% of the measured signal with the 16" spacing comes from within 0.5 m, which is about twice the boreholes' mean radius (Table 1). Here, measurements took place every 25 cm, with a logging speed of 1.8 m/min.

A total of eight measuring rounds took place but only four measuring rounds are presented in this study for NN-3 and NN-4 due to mainly one problem encountered on-site, related to the inability to inject current higher than 200 mA, happening randomly at certain places and dates (Table 2).

Traditional applications of the QL40-IP tool, e.g. in the mining industry, are typically fulfilled with 250 or 500 msec current injections (on-time) and a fixed number of 400 sample points in the whole cycle $T_{on,+}; T_{off,+}; T_{on,-}; T_{off,-}$. Two important differences between traditional applications and the present study led to the development of a new processing board. First, Martin et al. (2021) show that FDIP and TDIP data measured on the same samples decently overlap when current injections last at least 2 seconds during TDIP data acquisition. This overlap is key to quantifying pyrite volumes by Debye decomposition since these empirical relationships have only been established with FDIP data. Second, the 132 kV buried power line connected to the Nesjavellir power plant (Figure 2) is responsible for a strong 50 Hz signal in the TDIP data, as revealed by initial tests in NN-4 prior to this monitoring study (December 2019). These tests were carried out with the original QL40-IP tool, using 250-msec and 500-msec current injections, corresponding to full cycles of 1 and 2 seconds, respectively, and thus sampling rates of 400 and 200 Hz (400 sample points over the whole cycle). Using 2-second current injections, the full cycle lasts 8 seconds, which leads to a sampling rate of 50 Hz with 400 sample points and aliases the 50 Hz noise. Further investigations also showed that both the amplitude and exact frequency of the "50 Hz" noise varied over time. Therefore, it was clear that TDIP data acquisition with 2-second current injection required a larger number of sample points to model the noise and remove it before data analysis. This was achieved by increasing the memory of the processing board and led to an updated version of the QL40-IP tool used in the rest of this study.

From September 2020 (baseline) and on, the following IP acquisition settings were used: square-wave current injection ($T_{on,+}; T_{off,+}; T_{on,-}; T_{off,-}$ for 2 seconds each, 8 seconds total), 450 Hz sampling rate of the voltage during the whole cycle (i.e. 3600 sample points), and wireline speed of 1.8 m/min. The 50 Hz noise is further illustrated in Figure 3 (first and second columns).

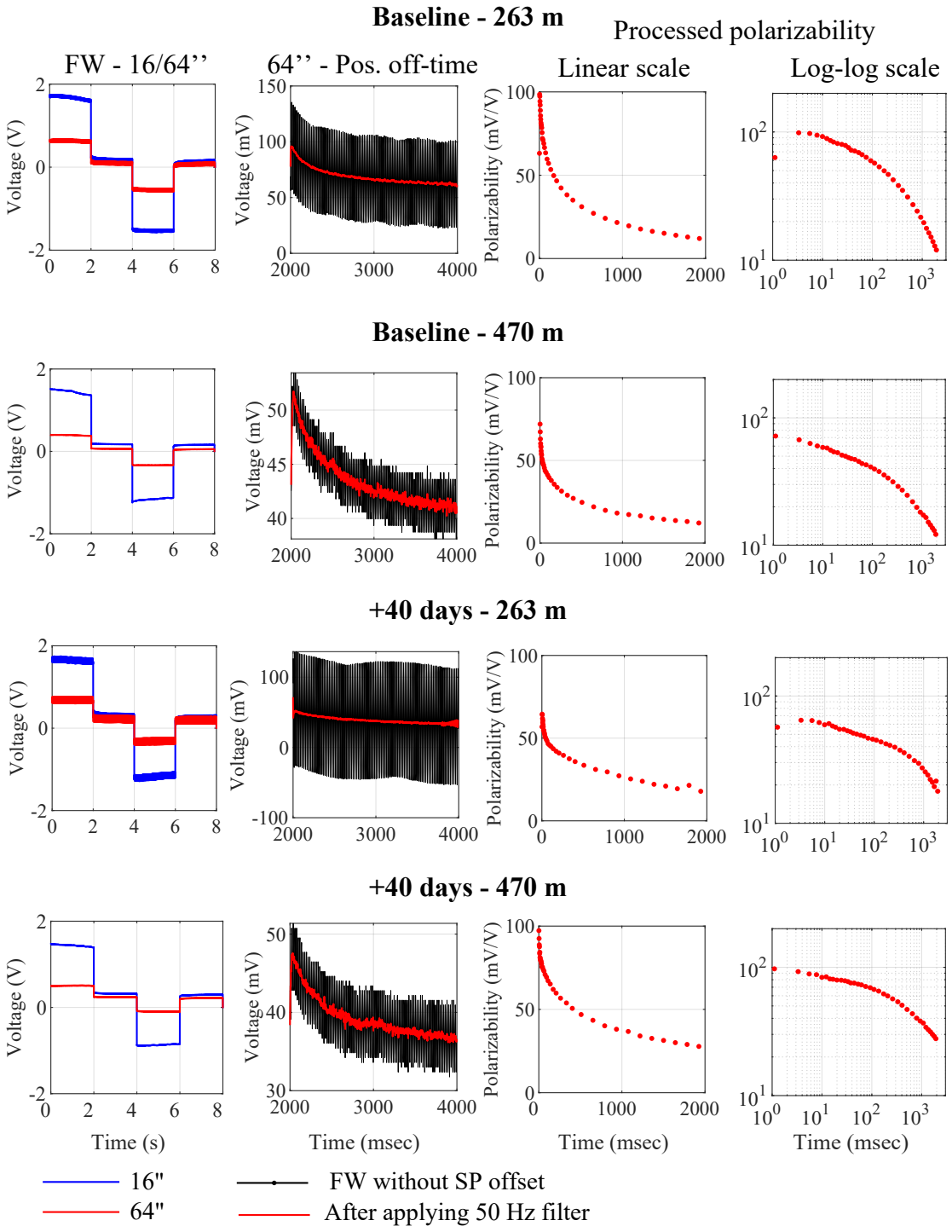

Figure 3. Full waveform (FW) TDIP data measured in NN3 with 16" and 64" electrode spacings (left column). The 50 Hz noise is further illustrated by zooming on the positive decay for the 64" data in the second column (signal in black), where the FW signal after removing the 50 Hz noise is also shown (in red). Further processing of the FW data into polarizability curves is shown in the third (linear scale) and fourth (log-log scale) columns. Results are shown at two different dates (baseline and +40 days) and two different depths (263 m and 470 m), showing varying levels of background noise.

Table 2. TDIP monitoring timeline and evaluation of data quality. "Good" means data quality was sufficient for further analysis.

Measuring date	NN-3	NN-4
December 2019 (preliminary)	no meas.	404 sample points
September 2020 (baseline)	good	good
March 2021 (+40 days)	good	good
November 2021 (+270 days)	good	current too low
February 2022 (+380 days)	current too low	good
July 2022 (+540 days)	good	good
October 2022 (+630 days)	current too low	current too low

In parallel to the TDIP monitoring, the changes in electrical resistivity were also monitored to evaluate the possible contribution of processes other than pyrite precipitation to the changes in the IP response. Indeed, changes in borehole fluid composition, temperature, and precipitation of clay minerals are reflected by changes in resistivity. Similarly, the formation of connected clusters of pyrite particles that would lose their polarization properties while becoming more conductive would also cause changes in the resistivity logs.

3.3 Data processing from full waveform voltage signal to polarizability decays

The apparent chargeability $M_{app}(t)$, also called polarizability and noted $\eta(t)$ in Martin et al. (2021) and Tarasov and Titov (2007), corresponds to the ratio between the decaying voltage during the off-time, $V_{decay}(t)$, and the maximum voltage reached during the on-time, V_{DC}. It is calculated by stacking positive and negative decays (equation 6).

$$M_{app}(t) = \eta(t) = \frac{V_{decay}(t)}{V_{DC}} = \frac{1}{2}\left(\frac{V_{decay,+}(t)}{V_{DC,+}} + \frac{V_{decay,-}(t)}{V_{DC,-}}\right) \tag{6}$$

A series of processing steps are carried out to clean the full waveform signal, optimize the signal-to-noise ratio, and maintain three time-decades of signal for the polarizability. The term polarizability is used in the rest of the paper to refer to the apparent chargeability defined in equation 6 in order to avoid confusion with the integral chargeability or the total chargeability parameter calculated from Debye decomposition.

First, a time-invariant self-potential (SP) voltage affects both $V(t)$ and V_{DC} in the positive and negative decays. The SP offset at each depth and each date is calculated by averaging the positive and negative DC voltages, $V_{DC,+}$ and $V_{DC,-}$ and removed from $V(t)$ and V_{DC}.

Second, harmonics of 50 Hz noise, due to a 132 kV buried power line, affect the voltage full waveform measurements, as mentioned in the previous section and illustrated in Figure 3. A power line noise model, based on the algorithm proposed by Larsen et al. (2022) and applied in a similar manner by Olsson et al. (2016), is used to subtract the harmonic noise from the signal. As shown by Larsen et al. (2022), the fundamental frequency varies over time, rapidly oscillating between 49.9 and 50.1 Hz, and must first be determined. The 2-second decaying voltage is thus decomposed into 200 msec segments, where the frequency is fitted in every segment. Once the exact frequency is determined, a model of the background noise, including harmonics up to Nyquist frequency, is removed from the signal. The denoised voltage after applying this 50 Hz filter is presented in Figure 3 (panels in the second column) as the red curve on top of the FW voltage (in black) during the positive off-time section of the full cycle.

Third, the voltage decays are re-gated into log-spaced time windows. This step transforms the full waveform voltage decay signal with 900 linearly spaced data points into a gated voltage signal with 37 logarithmically spaced gates. More accurately, the re-gated voltage consists of 10 gates in the first 22 msec (2.21 msec width, i.e., the original sampling step) and then exponentially larger gate widths (from 4.42 to 141.44 msec), over which an exponentially increasing number of data points (from 2 to 64) are averaged. Given the strong exponentially decaying shape in the early times, it appeared best to keep all data points in the first 22 msec. Since the original data points are kept as the 10 first gates, it corresponds to a "square-gate" with one data point averaged. To be consistent, the square gating strategy is kept throughout the decay. This is especially relevant because the signal can be locally approximated by linear functions in the later times. At some depths, the first gate (centered at 1.1 msec) is affected by electromagnetic (EM) coupling (see, for example, at +263 m in Figure 3). Therefore, it was discarded from all the re-gated discharge curves, and the first effective gate is at 3.32 msec: visual inspection of all the decays suggests that EM coupling is negligible at this gate, which is consistent with observations by Olsson et al. (2016).

Fourth, the positive and negative voltage decays are divided by the DC voltage and stacked to obtain the polarizability in mV/V (equation 6). The stacking allows removing extra noise with the same sign in the positive and negative decays. These four processing steps eventually provide the processed polarizability curves over almost three decades (in the range of 3-2000 msec), as presented in Figure 3 with a linear scale (third column) and log-log scale (fourth column). The linear scale allows better comparison to the full waveform signal presented in the same figure, while the log-log scale is used in the rest of this study.

Fifth, polarizability decays are averaged over 2-meter thick sections (Figure 4), corresponding to 8 decays averaged together (0.25 m spatial resolution). This is done to facilitate the comparison between measuring rounds since the exact depth of each single measurement varies at different dates. It also allows smoothing out short-wavelength signal oscillations that would prevent meaningful comparison between measuring rounds. The standard deviation corresponding to this average also captures noisy areas where the signal varies a lot over short distances. The averaging over 2-meter sections also takes into consideration the fact that logging measurements at one depth are, in reality, sensitive to a sphere around this given depth. Finally, averaging over 2-meter sections helps to identify and mitigate remaining harmonic noise.

Some polarizability curves remain noisy after the processing (non-monotoneously or non-exponentially decaying), e.g., at 263 m depth and +40 days shown in Figure 3 and at 382-384m and +40 days shown in Figure 4. Noisy processed polarizability curves are further addressed in the next subsection and discussed at the end of the paper.

3.4 Estimations of pyrite precipitation from polarizability decays

A simple way to represent TDIP data (polarizability decays) as a function of depth is to integrate the decays to obtain the so-called "integral chargeability", M_{int} (Mao et al., 2016; Telford et al., 1990). It represents the area enclosed by the discharge curve, $V(t)$, and its zero asymptote, in a given time-window, $[t1 : t2]$, divided by the primary voltage V_{DC} and the time-window width, as described by equation 7 (Bertin & Loeb, 1976; Sumner, 1976). An error on M_{int}, $Err(M_{int}9$, is calculated following equation 8 at every date d.

$$M_{int} = \frac{1}{t_2 - t_1} \int_{t_1}^{t_2} \frac{V(t)}{V_{DC}}\, dt \tag{7}$$

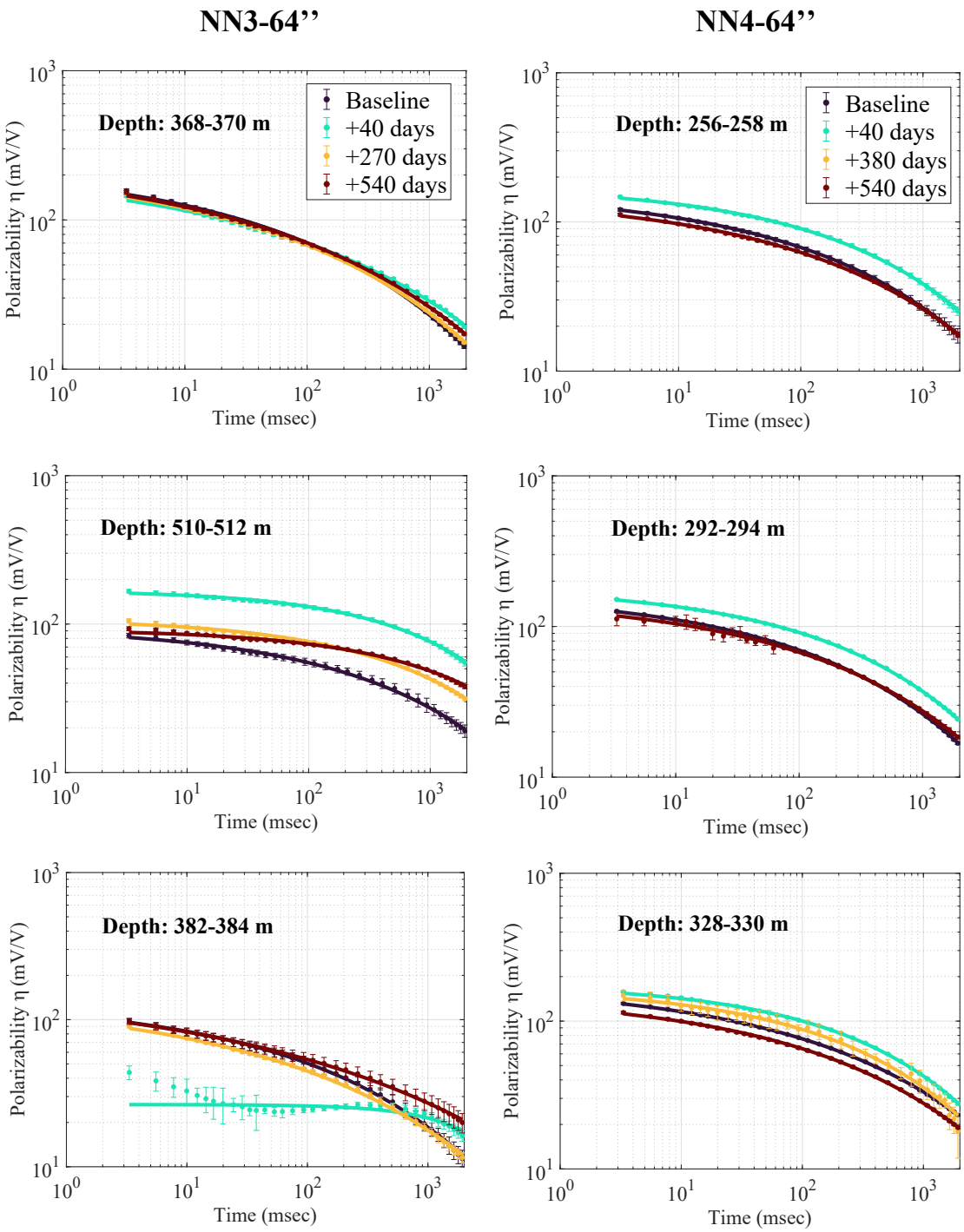

Figure 4. Resulting polarizability decays after the five processing steps. An example of noisy decay in NN3 is shown at 382-384 m depth, with larger error bars and a non-exponentially decaying shape.

$$Err(M_{int}(d)) = \frac{M_{int}(d)}{\overline{\eta}} \sqrt{\frac{1}{n}\sum_{i=1}^{n} std(\eta_i)^2} \tag{8}$$

where $std(\eta_i)$ is the standard deviation of the polarizability of the $i-th$ gate within the averaged 2-meter thick section, n is the number of time gates in the polarizability decays and $\overline{\eta}$ is the average polarizability over the n gates.

The integral chargeability presents the advantage of smoothing out the noise. It is calculated here in the time interval ranging from the second gate (3.32 msec) to the last gate (1926 msec). M_{int} is used in this study as a qualitative assessment tool of the change in polarization over time at a given depth, the trend corresponding to pyrite formation or dissolution. The error bar of the relative difference Δ_{rel} is calculated with equation 9 for the integral chargeability M_{int} and the resistivity ρ.

$$\begin{aligned} Err(\Delta_{rel} M_{int}(d)) &= \sqrt{(M_{int}(d) \cdot \frac{Err(M_{int}(d_0)}{M_{int}(d_0)^2})^2 + (\frac{Err(M_{int}(d))}{M_{int}(d_0)})^2} \\ Err(\Delta_{rel} \rho(d)) &= \sqrt{(\rho(d) \cdot \frac{Err(\rho(d_0)}{\rho(d_0)^2})^2 + (\frac{Err(\rho(d))}{\rho(d_0)})^2} \end{aligned} \tag{9}$$

where d and d_0 correspond to the current monitoring date and the baseline date, respectively, $Err(\rho(d))$ is the standard deviation within the averaged 2-meter thick section, and $Err(M_{int}(d))$ is calculated as per equation 8.

The integral chargeability calculated from TDIP data cannot be converted to pyrite volume as M_{int} is not equivalent to the "Cole-Cole" or "Pelton" m in equation 5. Several approaches have been developed to relate TDIP and FDIP data, considering there is no strict equivalence between Pelton models in frequency-domain and stretched exponential functions in time-domain (Alvarez et al., 1991). As described in section 2, there is an equivalence between the Debye decomposition calculated with FDIP and TDIP data, with a slight underestimation of m_{tot} from TDIP data when the current on-time is 2 seconds (Martin et al., 2021). Therefore, the conversion to pyrite volume fraction is carried out here by using Debye decomposition. The polarizability $M_{app} = \eta(t)$ is fitted by a non-negative linear least-square procedure, where the fitting function is given in equation 10 and the optimization problem is expressed in equation 11.

$$\eta(t) = \sum_{k=1}^{N} m_k e^{\frac{-t}{\tau_k}} \tag{10}$$

$$\min_{x \geq 0} \|Cx - d\|_2^2 \tag{11}$$

where x is a vector with the m_k model parameters, d is a vector with the measured data $\eta(t_i)$ and C is the linear multiplier defined as $C_{i,k} = e^{\frac{-t_i}{\tau_k}}$, where t_i are the center times of the p gates (i=1..p) and τ_k are the pre-defined N relaxation times (k=1..N). Here we define the $\tau_{k,k=1..N}$ as a set of $N = 300$ logarithmically-spaced values of relaxation times in the range $3-2000$, covering approximately three decades. During the procedure, most of the coefficients m_k are kept to 0 due to the non-negative constraints. The fit eventually results in 10-20 coefficients being non-zeros.

The total chargeability m_{tot} is calculated by summing all the m_k coefficients (equation 3). The difference of m_{tot} at different measuring rounds, Δm_{tot}, is converted into

a difference in pyrite volume fraction p_v, Δp_v, following equation 12, which is based on equation 5.

$$\Delta p_v(d)_{\%} = \frac{200}{9}[m_{tot}(d) - m_{tot}(d_0)] \tag{12}$$

where d and d_0 are the monitoring date and the baseline, respectively. Only the difference is converted, not the absolute pyrite volume fraction, in order to subtract the contribution of the background polarization that may be partly due to iron-oxides or other polarizable material present before the start of H_2S injection.

As opposed to the integral chargeability, the Debye decomposition seems to act as a noise amplifier, similar to observations by Martin et al. (2021). As mentioned previously, some polarizability curves remained noisy despite the numerous processing steps, with a resulting non-decaying shape. Such curves should not be processed with Debye decomposition. An additional processing step is introduced to ensure that only exponentially-decaying curves are processed with Debye decomposition. The criterion for ensuring this shape is based on the Kohlrausch-Williams-Watts relaxation model for TDIP data (Alvarez et al., 1991), presented in Appendix Appendix A. In practice, the polarizability curves $\eta(t)$ are fitted with a stretched exponential function, presented in equation 13, before applying the optimization procedure described in equations 10 and 11.

$$f(t) = \alpha e^{-(\frac{t}{\tau_{KWW}})^{\beta}} \tag{13}$$

The fitting parameters α, β, and τ_{KWW}, further described in Appendix Appendix A, are not used for interpretation in this study. Instead, the stretched exponential fit serves two purposes: (i) calculating a deviation to a stretched exponential to remove outliers polarizability curves where $R^2 < 0.998$ and (ii) smoothing out the polarizability decays that are reasonably deviating to ensure the Debye decomposition is not fitting noise. In order to confirm that this fitting procedure is not introducing a significant bias, the m_{tot} and τ_{mean} resulting from Debye decomposition before and after the fitting procedure are compared in Figures A1 and A2 in Appendix Appendix A. While other types of curves may reflect IP effects, with e.g. negative polarizability values having a physical explanation in the context of dipole-dipole acquisition with sharp layer boundaries (Fiandaca et al., 2022), the polarizability curves discarded here did not belong to these "heterodox transients", but rather had a distorted shape, similar to the curve in NN3 at +40 days at 382-384 m depth, presented in Figure 4.

An error is calculated on the resulting values of m_{tot} (equation 3), taking into account both the residuals to the stretched exponential fit and the standard deviation within the averaged 2-meter sections, to help discriminate between variations that fall within an uncertainty interval from significant variations over time. First, an error is calculated for each gate of the polarizability curve as the sum of the 2-meter standard deviation (corresponding to the variation within the averaged 2-meter section, see also equation 8) and the residuals to the stretched exponential fit (equation 14): if the residual is positive, it is added to the positive error bar err_+, if the residual is negative, it is added to the negative error bar err_-.

$$\begin{aligned} Err_+(\eta_{i,fit}) &= \begin{cases} std(\eta_i) + residuals(\eta_i, \eta_{i,fit}), & \text{if residuals}(\eta_i, \text{ fit}) > 0 \\ std(\eta_i), & \text{otherwise} \end{cases} \\ Err_-(\eta_{i,fit}) &= \begin{cases} std(\eta_i) - residuals(\eta_i, \eta_{i,fit}), & \text{if residuals}(\eta_i, \text{ fit}) < 0 \\ std(\eta_i), & \text{otherwise} \end{cases} \end{aligned} \tag{14}$$

where $\eta_{i,fit}$ is the value of the stretched exponential fit of the polarizability at the i-th gate, and Err_+ and Err_- are the positive and negative error bars on $\eta_{i,fit}$ at each gate.

Similarly to the error on M_{int}, a relative error is calculated for each decay using the root mean square of the error on all the gates divided by the average polarizability $\overline{\eta}$. This relative error is then applied to the total chargeability m_{tot}, then to Δm_{tot} (change from the baseline), and finally to the pyrite volume fraction change Δp_v, following equation 15.

$$
\begin{aligned}
Err_{rel} = \frac{1}{\overline{\eta}} \sqrt{\frac{1}{n} \sum_{i=1}^{n} \left(\frac{Err_+(\eta_{i,fit}) + Err_-(\eta_{i,fit})}{2}\right)^2} \\
Err(m_{tot}) = Err_{rel} \cdot m_{tot} \\
Err(\Delta m_{tot}(d)) = \sqrt{Err(m_{tot}(d))^2 + Err(m_{tot}(d_0))^2)} \\
Err(\Delta p_v(d)) = \frac{2}{90} \cdot Err(\Delta m_{tot}(d))
\end{aligned}
\tag{15}
$$

4 Results

4.1 Baseline resistivity and integral chargeability

In order to evaluate the amplitude and meaning of the changes in the following sections, the resistivity and integral chargeability measured in the baseline are first presented in Figure 5. The average resistivity of NN3 and NN4 is about 30 Ωm, with a clear threshold at 450 m in NN3, separating the well into two sections, above and below 30 Ωm. Both in NN3 and NN4, a few intervals have resistivity values significantly higher than 30 Ωm, up to 200 Ωm. These high-resistivity intervals coincide with low-chargeability intervals (gray rectangles in Figure 5). The average integral chargeability is around 20-30 mV/V, with generally higher values in NN4.

Intervals of higher resistivity correspond to more compact, less porous, lithological layers, where less hydrothermal fluid flow and thus alteration is expected (Lévy et al., 2018). Therefore, the relatively high chargeability in the baseline, as well as the coincidence of locally high resistivity with locally low chargeability, suggest that hydrothermal alteration had been occurring in the wells prior to the start of H_2S injection, especially in intervals of low resistivity. Small amounts of magnetite are expected in unaltered zones, typically 2-4 wt.% (Lévy et al., 2018) and may contribute to the chargeability in high resistivity layers (Lévy, Gibert, et al., 2019; Peshtani et al., 2022). Alteration minerals, such as pyrite and smectite, are especially expected in permeable, fractured layers (Lévy, Gibert, et al., 2019; Gudmundsson et al., 2010; Lévy et al., 2020) and may be responsible for the higher chargeability in low resistivity intervals, particularly below 450 m in NN3 and below 375 m in NN4. Note that smectite only contributes to polarization when present in small quantities, typically lower than 10% (Lévy, Weller, & Gibert, 2019; Telford et al., 1990; Mendieta et al., 2021), while it tends to decrease the overall polarization response at larger quantities (Lévy, Gibert, et al., 2019), as illustrated in Figure 1. Based on these observations, the interval below 450 m in NN3 is where extensive pyrite precipitation is expected following H_2S injection, which is also consistent with the observation that most of the "natural" hydrothermal alteration happens below 450 m in the area (Helgadóttir, 2021).

In both wells, higher chargeability is observed with the 64" spacing compared to the 16". Considering that the fluid is not chargeable in this frequency-range, this illustrates that the 64" images more volume of the chargeable properties of the rock formation, and thus more changes are also expected with the 64" spacing. On the other hand,

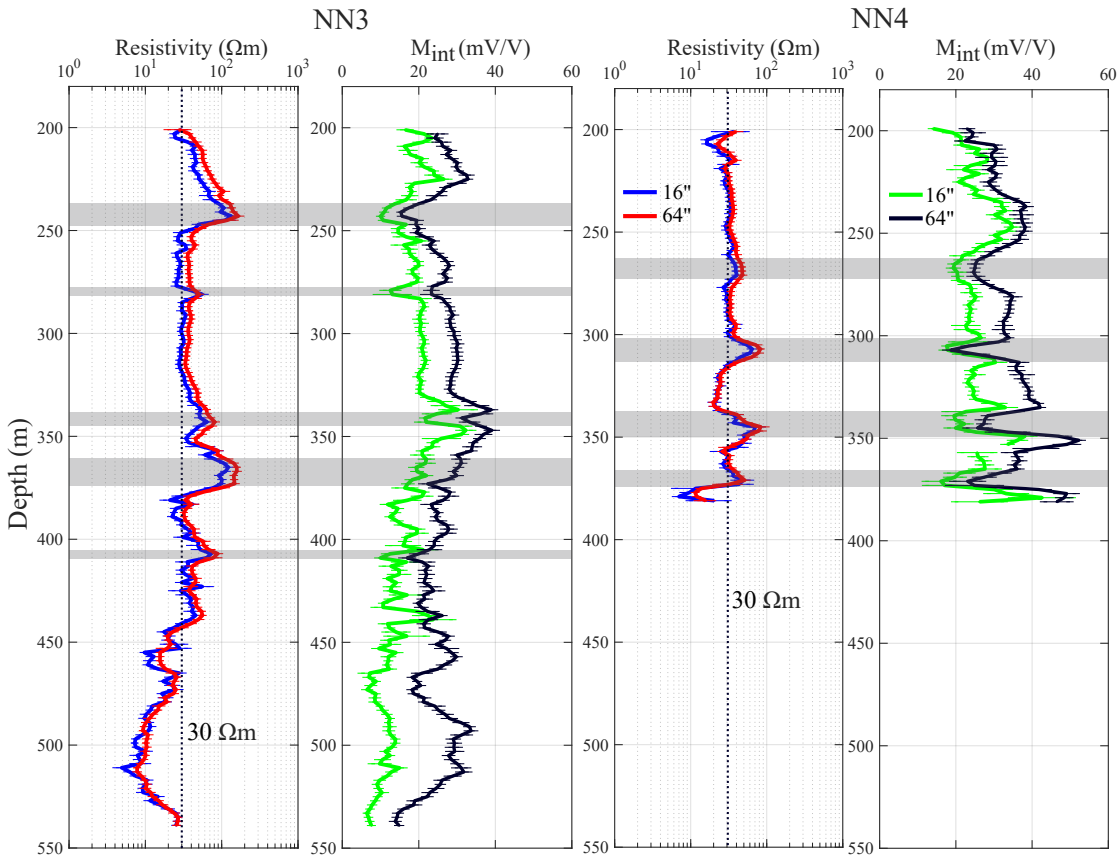

Figure 5. Resistivity (blue/red) and integral chargeability (green/black) logs in NN3 (left panels) and NN4 (right panels) using the 16- and 64" spacing (colors). All plots are based on an averaged signal every 2 meters, and the error bars correspond to the standard deviation within these 2-meter intervals. The dashed line shows the resistivity threshold of 30 Ωm. The gray rectangles indicate intervals with locally high resistivity and low integral chargeability.

similar resistivities are observed with both spacings, which reflects the fact that the fluid and the formation have resistivities in the same range. Based on fluid conductivity logging, the borehole fluid resistivity is around 10 Ωm in both wells (Table 1), i.e., only three times lower than the average 30 Ωm measured for the formation.

4.2 Changes in resistivity and integral chargeability over time

Logging results at +40 days (NN3 and NN4), +270 days (NN3), +380 days (NN4), and +540 days (NN3 and NN4) are presented as relative differences (in percentage), compared to the baseline in Figure 6. The average value within a 2-meter thick interval is taken for each round to smooth out rapid vertical variations. Error bars, calculated from the standard deviation of this 2-meter average (equation 9), allow discriminating significant changes over time from changes within the local variability. The resistivity after baseline is further corrected to remove the temperature effect, following equation 16 and using temperature logs shown in Figure B1 in order to assess resistivity changes reflect changes in porosity or clay content.

$$\frac{\rho(T)}{\rho(T_0)} = 1 + \alpha_T(T_0 - T) \tag{16}$$

where T and T_0 are the current temperature and the reference temperature (corresponding to the baseline temperature), respectively. And $\alpha_T = 0.02°C^{-1}$ is based on Arps (1953).

It can first be observed that changes depend on the electrode spacing for both the resistivity ρ and the integral chargeability M_{int}: relative differences are larger with the 64" spacing, indicating that more changes are happening in the rock formation than near the borehole wall (Figure 6). Resistivity variations are in many places within error bars, and thus, less focus is given here to interpret these variations.

Significant changes in the integral chargeability are observed. In NN4, M_{int} increases at +40 days by 10-20% with the 64" spacing and 5-10% with the 16" spacing (Figure 6). At the next monitoring date, i.e., +380 days, M_{int} decreases back to the baseline in most places with both spacings (note that data above 330 m were discarded for this date due to low current injected). At the last monitoring date, +540 days, M_{int} remains at baseline values down to 300 m, but the 64" signal decreases below baseline values between 300 m and the bottom of the well (380 m). The 16" signal mostly remains at baseline values all along the well. A similar trend is observed in the bottom part of NN3, below 450 m: first M_{int} increases at +40 days by up to 50% with the 64" and up to 20% with the 16" spacing. Then, M_{int} decreases for both spacings but remains above baseline values everywhere, unlike in NN4. At +540 days, below 450 m, slightly higher M_{int} values are observed compared to +270 days for the 64" spacing. The 16" signal follows the same trends everywhere, with lower amplitude. The maximum M_{int} increase is smaller in NN4 than in NN3, but the increase is more uniformly spread along the borehole in NN4. In particular, a significant increase is observed at +40 days in the whole well, i.e., between 200 and 380 m. In NN3, the most important changes are located between 450 and 550 m, with only minimal changes down to 450 m.

A consistent observation links the 16- and 64" spacing in NN3 and NN4: M_{int} does not follow a monotonous increase as would have been expected if pyrite had been precipitating continuously or even if pyrite had precipitated up to a certain amount and remained in place. To illustrate further the non-monotonous pattern observed in the four panels showing M_{int} variations in Figure 6, the evolution of M_{int} with time in certain depth ranges is presented in Figure 7 for NN3 and NN4, using only the 64" spacing (larger variations) and showing absolute differences in mV/V.

Resistivity changes in NN3 with the 64" spacing show a spatial correlation with M_{int} changes: a decrease of resistivity is observed in the upper part (above 450 m), and an increase is observed in the bottom part. As opposed to the time-evolution observed for M_{int}, the resistivity increase at the bottom of NN3 seems monotonous (Figure 6). In NN4, a resistivity decrease is observed at +380 days above 300 m, and an increase is observed between 300 and 350 m. However, an almost uniform resistivity decrease is observed at +540 days, both with the 64" and 16" spacing, which indicates that the fluid conductivity may have changed due to a change in fluid composition. Since the fluid conductivity was only measured at the last round (+540 days), further interpretation of the resistivity changes regarding porosity, cementation, or clay content would be uncertain.

Overall, this qualitative analysis of the monitoring results indicates that (i) the integral chargeability strongly increases at +40 days in both wells and tends to decrease at the following monitoring rounds, going back or close to the baseline, (ii) the integral chargeability increase at +40 days is rather uniform over the whole depth interval in NN4 (200-400 m), while the increase in NN3 is localized between 450 and 550 m and (iii) the resistivity tends to increase monotonously over time at the bottom (below 450 m) of NN3,

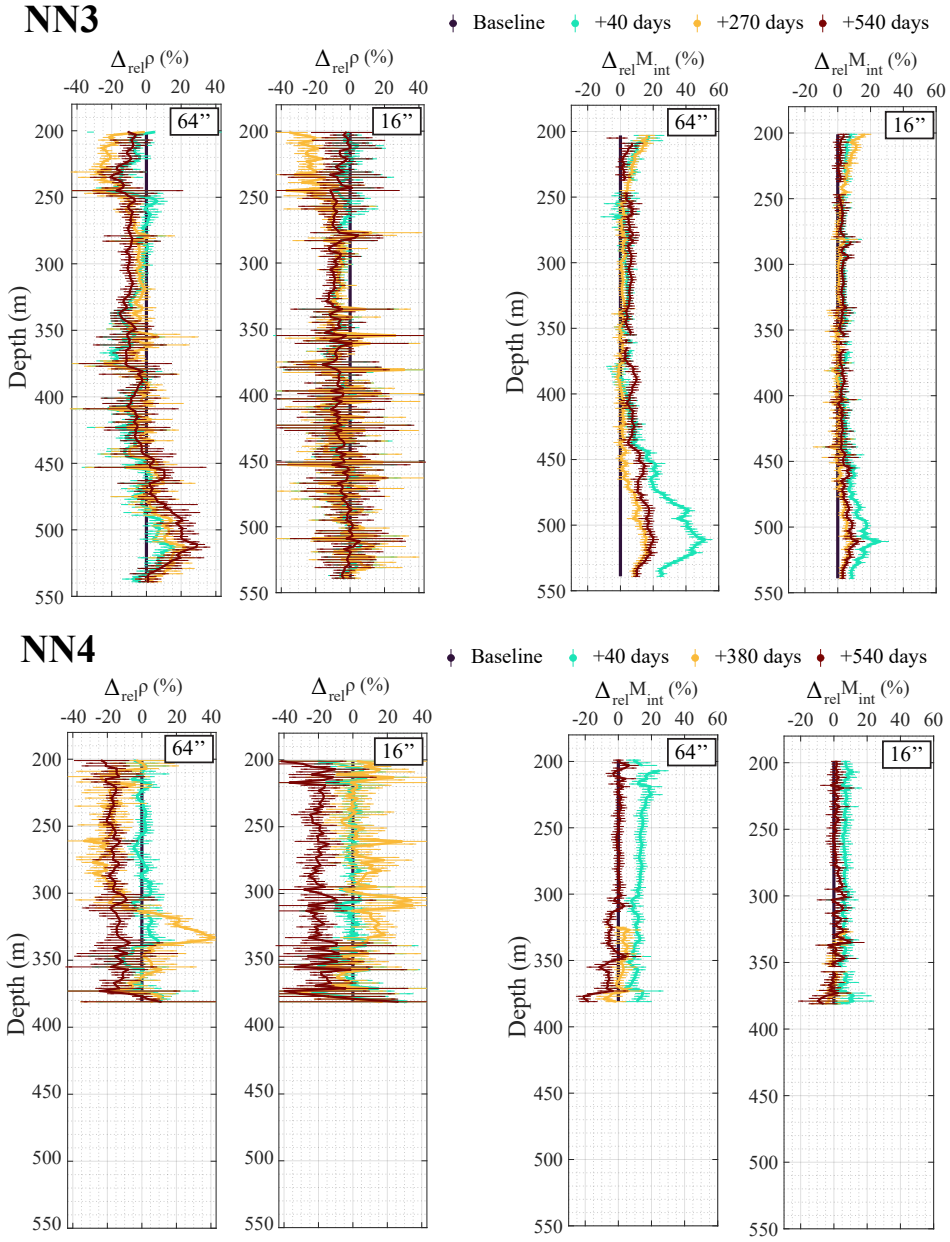

Figure 6. Relative difference of the temperature-corrected resistivity ρ (left) and integral chargeability M_{int} (right) in NN3 (top) and NN4 (bottom), for both 64" and 16" electrode spacing. Colors indicate the monitoring rounds.

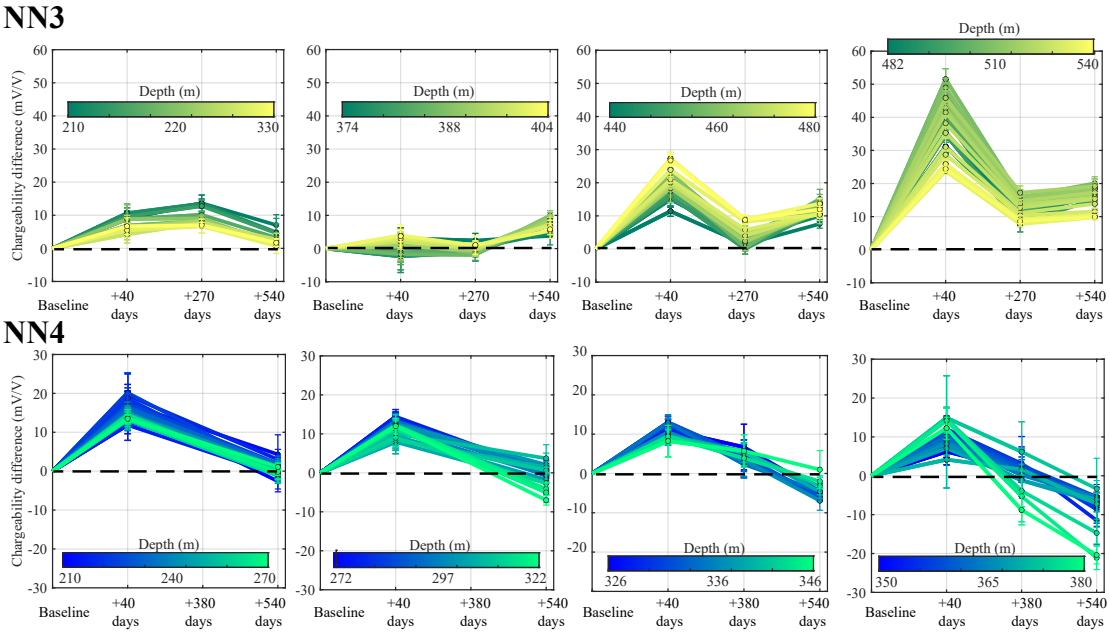

Figure 7. Evolution of the integral chargeability (absolute difference in mV/V) over time in NN3 (top) and NN4 (bottom) in different depth intervals, represented by the color scale. The dashed black line indicates the baseline level. Note the different scales for NN3 and NN4. Only data measured with 64" spacing are shown.

which may correspond to a decrease of porosity related to intense pyrite and secondary mineral precipitation, although impossible to quantify further.

In the following section, spectral information is extracted from TDIP monitoring results to allow a first-order quantification of pyrite precipitation in areas with an increase in M_{int}.

4.3 Extraction of spectral information through Debye decomposition

Since Debye decomposition tends to amplify the noise in the polarizability curves, decays that could not be fitted by a stretched exponential function (equation 13) with $R^2 \geq 0.998$ were discarded. This also smoothed out the decays that were kept and avoided fitting noise with the Debye decomposition. The theoretical justification and illustration of using a stretched exponential model for TDIP data is further described in Appendix Appendix A (Figures A1 and A2). Figure 4 also illustrates that the stretched exponential fit has minimal difference with the polarizability data in most cases.

Debye decompositions, illustrated in Figure 8 for two sets of decays in NN3 and NN4 (64" spacing), show a similar trend as observed in Figures 6 and 7. The polarizability decays at +40 days are above the baseline as well as the later monitoring rounds, both in NN3 and NN4. This trend is also reflected in the coefficients m_k, especially at long τ_k values, and the resulting m_{tot}, larger at +40 days. All Debye decompositions are available as figure sets S1 to S4 in Supplementary Information.

As can be seen on Figure A1, only 70% of the decays passed all the processing steps. Most affected datasets were at +380 days in NN4 (above 330 m) and at +40 days in NN3 (above 450 m). The noisy data above 450 m at +40 days is attributed to two factors that can be observed in Figure 3: (i) significantly stronger 50 Hz noise above 450 m than be-

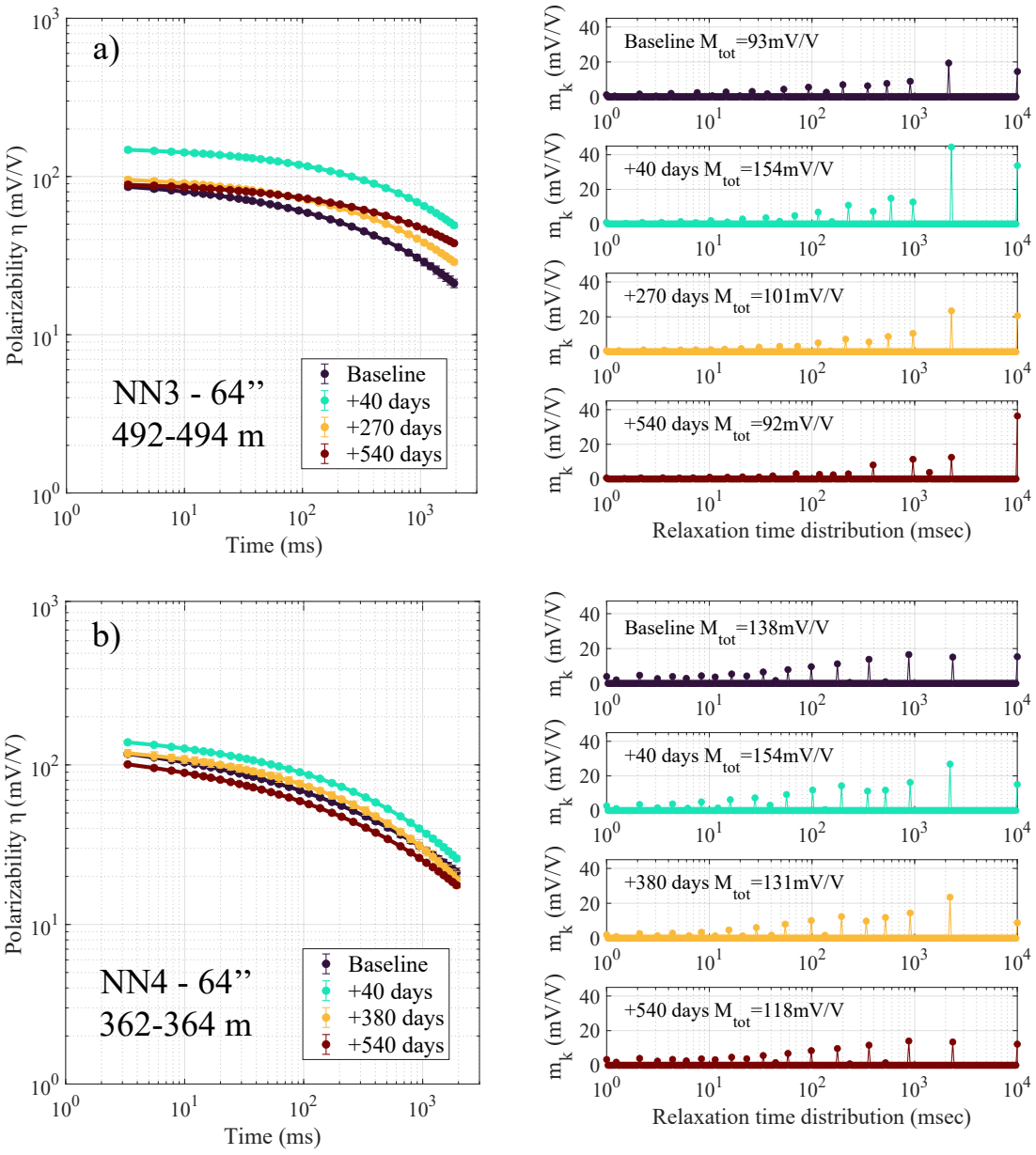

Figure 8. Debye decomposition for two sets of decays measured with the 64" spacing in a) NN3 at 492-494 m and b) NN4 at 362-364 m. Left: polarizability data and fit by the RTD function (equation 10); right: coefficients m_k for all the τ_k at the four measuring rounds.

low at all dates (reason unknown) and (ii) stronger 50 Hz noise at +40 days compared to baseline, at all depths. As can be observed in Figure 3, the signal level is always better with the 16" (blue) than with the 64" (red) electrode spacing, which is expected considering that the measured voltage decreases for increasing spacing with this configuration. This explains that fewer 16" data were discarded during the Debye decomposition filtering procedure (A1). However, the 64" data involve a larger depth of penetration around the borehole and are thus more relevant for conversion to pyrite volume change.

On the one hand, the integral chargeability presents the advantage of smoothing out noise and providing a qualitative overview of the trends for the whole dataset. On the other hand, Debye decomposition allows extracting spectral information and further quantifying pyrite volume fraction change. Ideally, a unique relation would exist between m_{tot} values obtained by Debye decomposition and the integral chargeability M_{int}, which would allow to convert M_{int} into pyrite volume fraction. However, we find that different relations exist between m_{tot} and M_{int}, depending on the mean relaxation time. Investigating further these relations is beyond the scope of this study. Thus, pyrite estimations in the next section are calculated on a reduced portion of the dataset, where Debye decomposition was carried out.

4.4 Quantification of pyrite volume fraction change

The absolute difference in total chargeability, Δm_{tot}, further converted into Δp_v are presented in Figure 9 for the three monitoring rounds. While the same trends are observed as in Figure 6, this conversion allows estimating the extent of pyrite precipitation or dissolution. Error bars also differentiate between significant differences in pyrite volume fraction versus differences too uncertain to be interpreted further. Overall, precipitation of up to 2% and 1% are observed with the 64" and 16" electrode spacing, respectively. Figure 9 illustrates that more volume fraction changes are observed when taking into consideration a larger volume around the boreholes, which emphasizes once more that changes are not limited to the very near vicinity of the injection boreholes.

In NN4, an increase in pyrite volume fraction at +40 days (+0.5-1% compared to baseline) is observed with both the 16" and 64" electrode spacings at all depths, followed by a decrease at +380 and +540 days. In addition, the 64" data indicate that the decrease at +540 days extends below baseline values (-0.2-0.5% compared to baseline). In NN3, changes are more depth-dependent than in NN4. Between 200 and 450 m, no significant changes are observed at any rounds. However, it is important to note that, at +40 days, most of the 64" data in this depth-range were discarded during the Debye decomposition filtering procedure. Below 450 m, all the way down to 550 m, +1-2% in the pyrite volume fraction is suggested by the 64" data and +0.5-1% by the 16" data. At +380 and +540 days, the 64" and 16" data, where available, suggest a decrease towards baseline values, yet never extending below baseline values, as opposed to NN4.

4.5 Analysis of the mean relaxation time

Overall, relaxation times are shorter in NN4 than in NN3, with a maximum of 300 msec in NN4 and above 1000 msec in NN3 (Figure 10). It can also be noted that the variations of the average relaxation times across the different monitoring rounds follow the variations of m_{tot}. In NN3 below 450 m, τ_{mean} increases at +40 days and decreases back at +270 days. In NN4 across the whole well, τ_{mean} increases at +40 days and decreases back at +270 days. In NN3, significantly longer relaxation times are observed below 450 m, which reflects the different shape of the polarizability decay curves, with most of the decay happening at late times, as opposed to depths above 450 m. Similarly, in NN4, decays at 346-348 m and at 380-382 m have a different shape and correspond to minimum and maximum values of τ_{mean} over the whole well, 40 and 400 msec, respectively.

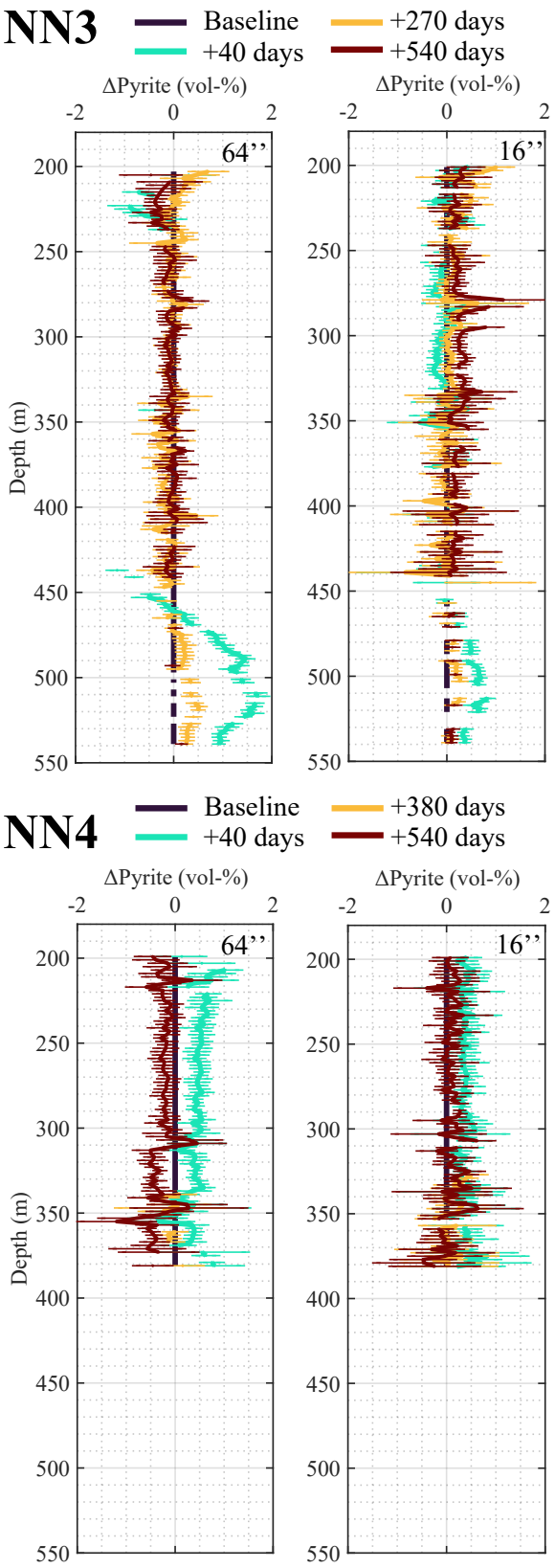

Figure 9. Estimations of pyrite fraction change (absolute difference of pyrite vol-%) in NN3 (top) and NN4 (bottom), based on TDIP logging with 64" and 16" electrode spacing, using Debye decomposition of the decays.

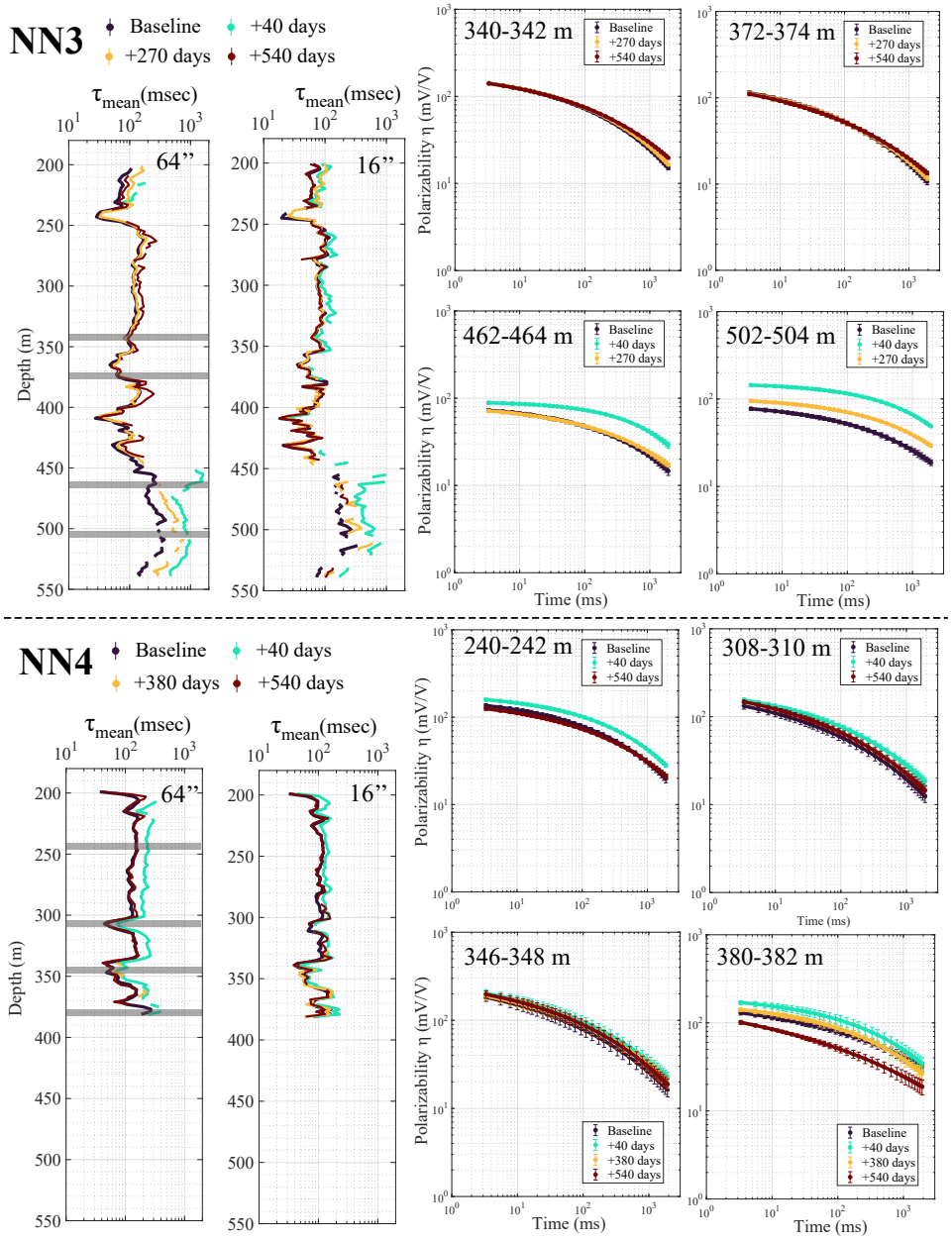

Figure 10. Left: mean relaxation times, τ_{mean}, from Debye decomposition in NN3 (top) and NN4 (bottom), for both the 64" and 16" spacings, at different monitoring rounds. Polarizability curves for four selected depths for each well, using the 64" spacing. The corresponding depths are shown on the depth-τ_{mean} plots with gray rectangles.

As was observed in Figure 1, longer relaxation times, corresponding to lower frequencies, can be associated with either larger metallic grain sizes or connected metallic grains, e.g., forming veins. In this case, relatively small pyrite grain sizes are expected due to the short time available, especially after +40 days (around 10 μm according to laboratory experiments presented by (Prikryl et al., 2018)). Therefore, long relaxation times in NN3, below 450 m, may indicate connected pyrite particles in fractures. On the other hand, shorter relaxation times in NN4 may be associated with small, disseminated pyrite particles.

It is important to note here that TDIP data are only capturing polarization processes associated with relaxation times larger than 3 msec, which is above the typical range of relaxation times investigated by FDIP laboratory studies, such as Martin and Weller (2023) and (Revil, Abdel Aal, et al., 2015). Therefore, converting the relaxation time distributions into grain size distribution would be uncertain.

5 Discussion

5.1 Interpreting subsurface processes behind the monitored resistivity and TDIP responses

First, the justification for converting total chargeability into pyrite volume fraction changes is discussed here. This conversion assumes that pyrite precipitation is the process governing the increase in chargeability. Based on reaction path modeling carried out in similar conditions, it is likely that some amount of smectite precipitates (Galeczka et al., 2022). Still, smectite precipitation is expected to have little influence on the IP signal in the presence of pyrite and could not alone explain the observed chargeability increases (Lévy, Gibert, et al., 2019; Lévy, Weller, & Gibert, 2019; Revil et al., 2017). Precipitation of iron-(oxyhydro)oxides following basalt dissolution is also possible, but only magnetic iron-oxides, such as magnetite or ilmenite, yield a strong polarization response (Peshtani et al., 2022). In these conditions, only non-magnetic Fe(III)-bearing phases are expected, such as goethite or hematite, based on laboratory experiments (Menefee et al., 2018; Andreani et al., 2009), field-scale modeling (Galeczka et al., 2022), and the general low-temperature alteration sequence of Icelandic basalt (Crovisier et al., 1992; Arnórsson et al., 1983; Gunnlaugsson & Arnòrsson, 1982; Stefánsson & Gíslason, 2001). In addition, amorphous silica and other silica-based minerals, such as quartz and zeolites, are expected (Daval et al., 2011; Galeczka et al., 2022). Amorphous silica, zeolites, and Fe(III)-bearing phases further have a strong tendency to clog the pore space (Menefee et al., 2018; Andreani et al., 2009), without creating a distinctive polarization signal (Revil et al., 2002). Finally, the influence of microbial activity on the IP response is still poorly understood but seems to yield polarization of much smaller amplitude than the observed changes (Mellage et al., 2018) and will therefore not be considered here.

With these considerations in mind, TDIP monitoring brings three types of insights: spatial variability, long-term evolution, and quantity of pyrite volume changes.

The spatial variability of pyrite precipitation is assessed as a function of depth, variability between NN3 and NN4, and distance from injection well. First, it is clear that more pyrite precipitation occurs in the depth range 450-550 m in NN3 than in the rest of the well, while in NN4, rather uniform pyrite precipitation is inferred (Figures 6 and 9). This can be understood in light of the baseline resistivity (Figure 5), showing resistivity lower than 30 Ωm at levels deeper than 450 m in NN3. In this 450-550 m interval, more clay content was found at the time of drilling (Helgadóttir, 2021), indicating preferential hydrothermal flow. While the injection rate is ten times larger in NN4 than in NN3 (Table 1), more precipitation seems to occur at the bottom of NN3 compared to NN4. This may be due to fracture flow transporting the H_2S-rich fluid rapidly away in NN4, not allowing time for pyrite precipitation. This would be consistent with the over-

all lower resistivity in NN4 in the common depth interval 200-380 m, compared to NN3 (Figure 5), and would mean that there exists an optimal permeability that maximizes the volumetric change in pyrite, ensuring at the same time ample fluid supply (H_2S supply) and sufficient fluid residence time (basalt dissolution).

Second, it can be inferred that more precipitation occurs away from the well than on the borehole walls, based on the comparison between the 64" and 16" datasets in both wells (Figure 6).

The time-evolution of resistivity, integral chargeability, total chargeability and mean relaxation time show that subsurface processes may be more complex than the expected continuous pyrite precipitation suggested by previous studies (Clark et al., 2020; Gunnarsson et al., 2018). Integral chargeability time-series presented in Figure 7 show that in both wells, at most depths, the initial increase at +40 days is followed by a decrease, extending below baseline values in NN4 at depths below 330 m. This trend, which is common to the 64" and 16" spacings (Figure 6), is also observed with the total chargeability and relaxation time (Figures 10, 9 and A1). Here, three different interpretations are explored: (i) pyrite is still precipitating after +40 days, but the IP signal decreases anyway, (ii) previously formed pyrite grains are "passivated" by a coating layer of secondary minerals preventing polarization while no more pyrite is forming and (iii) pyrite is being re-dissolved.

Interpretation (i) would be consistent with the observation by Martin and Weller (2023) that the same amount of pyrite, with increasing grain size, yields a lower IP signal. However, the relaxation time, which is the main indicator for particle size (Figure 1) also starts decreasing after +40 days (Figure 10), which indicates that pyrite particles, if they are still there, are not growing in size. This interpretation is, therefore, ruled out.

Interpretation (ii) is based on the fact that strong polarization effects are caused by metallic particles only when they have a clean surface. If secondary minerals isolate the pyrite surface from the fluid, the particles are passivated, and the polarization decreases (Gurin et al., 2019). Amorphous silica and Fe(III)-bearing minerals are common coating layers, which may coat pyrite grain surfaces, as well as reduce basalt dissolution rates by coating fresh basalt and clogging the pore space (Menefee et al., 2018; Andreani et al., 2009; Daval et al., 2011). Corrosion of pyrite surface in the presence of little amounts of oxygen may also lead to a similar passivation effect, without significantly dissolving the pyrite particle (Placencia-Gómez et al., 2013).

Interpretation (iii) contradicts the common idea that pyrite mineralization is stable in this context once formed. However, practical field conditions differ from typical hypotheses in reactive transport models, which are constrained by the availability of suitable frameworks and databases. Firstly, a high disequilibrium near the borehole, where H_2S-rich fluids are constantly injected, makes conventional „steady-state“ assumptions irrelevant. Secondly, previous experiments on CO_2 injection in basalt at Hellisheiði (similar set-up as the Nesjavellir field case presented here) triggered a bloom of iron-oxidizing bacteria, such as *Gallionellaceae*, and more generally sulfur- and iron- oxidation markers (Trias et al., 2017). At Nesjavellir, provided that oxygen was present in the system at some point (which could be the case due to e.g., leakage in the pipe system happening at the beginning of the H_2S injection), specific microbial communities may have developed and triggered pyrite oxidation (Mielke et al., 2003; Percak-Dennett et al., 2017). The fracture networks that are ubiquitous in basaltic rocks could also be a pathway for intermittent oxygen delivery, which would extend the depth of the habitable zone for iron-oxidizing bacteria (Bochet et al., 2020). Overall, biologically-driven mechanisms, which could explain an unexpected pyrite dissolution over time, are not taken into account in previous studies claiming that pyrite mineralization is stable due to the difficulty of representing them correctly in reactive transport simulations. While high-temperature geother-

mal systems may prevent the development of most microbial communities, the shallow system studied here has a relatively low reservoir temperature, although the injected fluid temperature is higher (Table 1).

The pyrite volume fraction change estimated in Figure 9 assumes, to simplify, that all the decrease of chargeability is explained by pyrite dissolution. In practice, there may be a mix of passivation and re-dissolution and, thus, a more conservative interpretation of the vol.% presented in Figure 9 would be the change in pyrite volume fraction contributing to the IP signal. While it is impossible from geophysical data alone to determine whether passivation (interpretation ii) or re-dissolution (interpretation iii) are responsible for the observed signals, both could be further investigated by laboratory studies, as well as by installing a more continuous geophysical monitoring infrastructure.

In addition to the uncertainty on the source of polarization decrease, the quantification of pyrite volume presents additional uncertainty. It should first be noted that the influence of background polarization not related to sulfide minerals in the baseline (Figure 5) is managed by only converting the difference of total chargeability between different monitoring rounds into the difference in pyrite volume fraction. However, equation 5 proposed by Revil, Florsch, and Mao (2015) and used here presents other limits, as Martin and Weller (2023) found that the exact relation between m_{tot} and p_v depend on the grain size of pyrite particles. Furthermore, the use of an equation calibrated with FDIP measurements to convert TDIP measurements is made possible by "long" current injections (2 seconds), where the TDIP and FDIP responses are supposed to overlap (Martin et al., 2021). However, 2-second current injections remain short, compared to 64"second used by Martin et al. (2021) to show the equivalence with laboratory measurements. Therefore, the pyrite difference calculated here from 2-second TDIP data is certainly underestimated. It was also assumed here that, at a given depth, precipitation occurs uniformly over a certain (undetermined) lateral extent, considered representative of near-borehole conditions. Further modeling of the contribution from the different cylindrical layers around the borehole to the measured signal, and thus of the pyrite volume in each of these layers, could be achieved with inversion.

Finally, it is interesting to note that the mean relaxation time is not only time-dependent but also depth-dependent and that an overall consistency of the decay shapes at a given depth is seen over time (Figure 10). This suggests that the local lithology and fracture network influence the relaxation time, most likely by influencing the patterns for pyrite precipitation. Although this is purely speculative, it may have implications for a better understanding of fracture networks in subsurface storage systems.

5.2 Requirements and added-value of IP-logging compared to current practices

As mentioned in the Introduction, current monitoring of field-scale H_2S reinjection, and similarly of CO_2 reinjection, have major pitfalls: (i) tracer tests capture less than 5% of the gas migration flow (Matter et al., 2016), (ii) mass balance calculations assume that the amount of sulfur not captured by downstream measurements, compared to expectations based on tracer tests, has mineralized into sulfide minerals (Gunnarsson et al., 2018) and (iii) long-term predictions by reactive transport models are not calibrated by field monitoring and thus present significant uncertainty (Ratouis et al., 2022; Aradóttir et al., 2012; White et al., 2020). Little has been researched on the long-term stability of the newly formed minerals in a context where the continuous injection of H_2S (and similarly, CO_2) creates a constant disequilibrium in the system, in terms of acidity and redox conditions in particular. Overall, current monitoring approaches are still indirect and cannot physically confirm the presence, location, and quantity of expected minerals in the rock matrix, nor their long-term stability. The results presented here show the feasibility of monitoring pyrite precipitation with logging TDIP chargeability measure-

ments within injection wells. However, several conditions/constraints/obstacles need to be overcome.

To start with, an appropriate tool is required. Compared to more conventional applications of TDIP, typically in mining exploration, the expected polarization signal is weaker (smaller volumes of sulfide minerals). At the same time, the presence of power lines due to the proximity to the power plant creates a significant 50 Hz background noise. Therefore, large current injection is essential to ensure a sufficient signal-to-noise ratio, and the acquisition of voltage with a high sampling rate is essential to separate the contribution from 50 Hz noise and from the rock to the voltage waveform. In addition, the need for quantification of pyrite precipitation, and thus comparison to frequency-domain IP calibrations, requires that current injection and voltage acquisition happen over a sufficiently long time to capture the polarization information needed for the interpretation. All these specifications required the development of new hardware in the existing QL40-IP instrument. In particular, the need for both longer injection/acquisition time and a higher sampling rate means that more data needs to be collected and recorded in the instrument's memory. The instrument went from recording 100 samples per cycle (depth) to 980. Nevertheless, a trade-off was adopted, and the current waveform, deemed less critical for the analysis, was not recorded; only the average current at each depth was recorded. In addition, the maximum injection/acquisition times were 2 seconds. Ideally, recording the current full waveform, injecting during longer times, and combining different injection times would allow a more accurate comparison to FDIP calibrations.

Field conditions are also important to consider to carry out successful TDIP logging. The instrument has a temperature limit of $70°C$, and its exposure to corrosive fluids shall be limited. This can be challenging in the context of CO_2 and H_2S injection wells at geothermal sites. On the other hand, injection wells are the location with strong changes in mineralogy. At the Nesjavellir site, the need to stop the injection and cool down the wells a few days before the measurements represented the main obstacle to repeating the measurements more regularly. In addition, the method requires an operator on-site to operate the instrument. In this context, where data redundancy is limited while TDIP measurements are easily subject to noise, data loss is a critical aspect to manage, especially for quantitative conversion.

Despite field limitations and remaining uncertainties, IP-logging monitoring brings novel insights into the processes at play, as emphasized in the previous subsection. A possible way forward would be to carry out the logging in dedicated monitoring wells relatively close to the injection wells to avoid the financial and environmental cost of stopping the injection during monitoring. Another possibility that would also fulfill the need for more continuous data acquisition to overcome episodic data losses would be the installation of permanent electrodes in dedicated wells. The electrodes would connect to an instrument remaining at the surface during the whole monitoring period, and only batteries would need to be changed periodically. Furthermore, this approach could allow 2D or 3D monitoring if several wells are used together in a cross-borehole electrical tomography approach. External data acquisition would also be helpful to further elucidate the physical processes behind the observed IP response. Monitoring the fluid conductivity over time appears essential to assess changes in fluid composition and further interpret resistivity changes. Complementary logging methods may include sonic and density logging for assessment of porosity changes, acoustic televiewer, and spinner logs for mapping fractures and flow paths, and color optical camera for direct observations of the precipitation of pyrite and biofilms at the borehole wall.

5.3 Can the IP-logging method be applied for monitoring other reactive processes?

Due to the strong signal caused by sulfides and other metallic minerals (Pelton et al., 1978), mapping ore deposits is still the main industrial application of IP methods today. Here, we present the first field example where reactive processes involving the precipitation and/or dissolution of metallic minerals are monitored with IP-logging. Other field examples for monitoring, with IP methods, reactive processes involving metallic minerals include the immobilization of uranium contamination by stimulating iron and sulfate-reducing microorganisms (Flores Orozco et al., 2011) as well as the injection of zero-valent-iron amendment to aid bioremediation of chlorinated solvents (Flores Orozco et al., 2015). In these examples, surface TDIP is used, and the limited spatial and temporal resolution complicates the interpretation. There, IP-logging could help improve the understanding of physical processes at play.

Studies on the link between IP and bacterial activity often find that microbially-mediated metallic minerals cause an IP response (Williams et al., 2005; Flores Orozco et al., 2011; Slater et al., 2007). However, recent studies suggest that polarization of bacterial cells themselves may control the IP response in certain cases (Mellage et al., 2018; Strobel et al., 2023). Therefore, in addition to monitoring the bioremediation of contaminants, IP-logging could also be applied to the study of microbial life in a dynamic natural environment, such as intermittent oxic–anoxic fluid mixing in fractured rocks (Bochet et al., 2020), provided that upscaling issues can be overcome (Mellage et al., 2018).

Finally, we evaluate to what extent the method developed here could be applied to monitoring CO_2 injection in basalts. Laboratory studies suggest that calcite precipitation causes significant polarization increase (Wu et al., 2010). However, others observe limited polarization increase, or even a decrease, in response to calcite precipitation (Wu et al., 2011; Zhang et al., 2012; Saneiyan et al., 2018) as well as no decrease associated with calcite dissolution (Halisch et al., 2018). Recent studies attribute these contradictory findings to the dominating influence of pore water chemical changes or dissolution changes on the IP response (Rembert, 2021; Izumoto et al., 2020). Therefore, the current petrophysical knowledge on the electrical response of calcite is insufficient to allow direct mapping of calcite in the field with IP methods. Nevertheless, H_2S is often associated with CO_2 in emissions from geothermal or coal power plants (Wang et al., 2011; Fridriksson et al., 2016). H_2S is often considered an impurity and is only injected with CO_2 to minimize the cost of separation. Still, the formation of pyrite could be used as a marker of mineralization processes, given that pyrite and calcite precipitations are primarily controlled by basalt dissolution rates (Prikryl et al., 2018; Stefánsson et al., 2011) and also share similar kinetics (Plummer et al., 1979; Williamson & Rimstidt, 1994).

6 Conclusions

To date, monitoring efforts of an implemented field-scale H_2S reinjection system have only occurred via concentration measurements, mass balance calculations, and analysis of precipitates on submersible pumps in injection and downgradient boreholes. These studies, along with geochemical numerical models and laboratory simulations, concluded effective H_2S sequestration through pyrite formation. Borehole sampling of fluids, although effective at identifying the occurrence of sulfide mineralization, provides limited quantitative, spatial, and temporal information on in-situ sulfide mineralization.

In order to bring insights into the subsurface physical processes controlling mineralization in the context of H_2S injection in basalts, as well as quantitative information on the sulfide mineralization in a specific case, a "shallow" (200-550 m) injection of H_2S at Nesjavellir geothermal field was monitored by means of resistivity and time-domain induced polarization wireline logging. Pyrite precipitation was expected to affect primar-

ily the induced polarization signal, while other changes (e.g., fluid conductivity, temperature, clay minerals precipitation) were expected to affect the resistivity.

The QL40-IP logging tool, developed by the company Advanced Logic Technology, was modified to allow longer current injection and a larger sampling rate than previously. This was needed to filter a strong 50 Hz background signal due to the proximity of a buried power line and convert the TDIP data into sulfide volumes using a laboratory-based relationship.

The first logging measurements were carried out in the summer of 2019, and the baseline with the modified tool was measured in September 2020. H_2S injection began on January 29th, 2021. After the start of injection, five logging monitoring rounds (+40, +270, +380, +540, +630 days) were carried out in wells NN3 and NN4. Out of these five rounds, only three remained for each well due to too low current injected in the other rounds for unknown reasons.

Monitoring results show that polarization strongly increases at +40 days in both wells and tends to decrease at the following monitoring rounds, going back close to the baseline or below. The polarization increase is rather uniform over the whole depth interval in NN4 (200-400 m), while the increase is clearly localized between 450 and 550 m in NN3, where more hydrothermal alteration was also found prior to the injection of any wastewater. Conversion of chargeability absolute difference into pyrite volume fraction change indicates precipitation of up to 1% in NN4 and 2% in NN3 at +40 days. In both wells, changes are more pronounced with the larger electrode spacing (64"), indicating that pyrite precipitation takes place away from the well.

The decrease of chargeability observed in both wells at +270 and +380 days suggests that pyrite is either passivated or re-dissolved after precipitating. The presence of specific microbial communities that can produce oxygen at these depths should be further investigated. Recommendations for future monitoring include: (i) installation of permanent monitoring systems to better understand the trends, (ii) considering the possibility of pyrite re-dissolution in reactive transport modeling of H_2S sequestration, and (iii) validation of geophysical results by additional in-situ measurements and observation, such as color camera and multi-level water sampling in wells.

7 Open Research

The TDIP data used for monitoring H_2S fate in the study, together with the resistivity, fluid conductivity and temperature data, will be available on the following Zenodo repository at the time of publication (Lévy, 2023): `https://doi.org/10.5281/zenodo.10145643` with Creative Commons Attribution 4.0 International license. For review purposes, data are shared as supplementary information.

Acknowledgments

The logging crew at ÍSOR is thanked for the numerous logging campaigns: Halldór Ö. Stefánsson, Halldór Ingólfsson, Friðgeir Pétursson. Jakob J. Larsen is thanked for their very appreciated help with signal processing. Thus S. Bording, Pradip K. Maurya, and Gianluca Fiandaca are thanked for all the valuable discussions around the processing and interpretation of TDIP data. Ásdís Benediktsdóttir, Vala Hjörleifsdóttir, Íris E. Einarsdóttir and Bjarni S. Gunnarsson are thanked for their help in organizing and coordinating logging campaigns with the power plant. Iwona Galeckza, Helga M. Helgadóttir, and Sveinborg H. Gunnarsdóttir are thanked for numerous discussions around the geology and geochemistry at Nesjavellir. LL received funding for the GEMGAS project from the Technological Innovation Fund, Tækniþróunarsjóður, at the Icelandic Center for Research, Rannsóknamiðstöð Íslands (grant no. 198637-0611). DC received a PhD grant from the

Nordic Center for Volcanological research, Nordvulk. AW acknowledges the support of Deutsche Forschungsgemeinschaft through grant no. 425975038.

References

Abdulsamad, F., Florsch, N., & Camerlynck, C. (2017). Spectral induced polarization in a sandy medium containing semiconductor materials: experimental results and numerical modelling of the polarization mechanism. *Near Surface Geophysics*, *15*(6), 669–683.

Advanced Logic Technology. (2021). *User guide: Ql40 elog/ip – normal resistivity and induced polarization probe* [Generic].

Alvarez, F., Alegra, A., & Colmenero, J. (1991, Oct). Relationship between the time-domain kohlrausch-williams-watts and frequency-domain havriliak-negami relaxation functions. *Phys. Rev. B*, *44*, 7306–7312. Retrieved from `https://link.aps.org/doi/10.1103/PhysRevB.44.7306` doi: 10.1103/PhysRevB.44.7306

Andreani, M., Luquot, L., Gouze, P., Godard, M., Hoisé, E., & Gibert, B. (2009). Experimental study of carbon sequestration reactions controlled by the percolation of co2-rich brine through peridotites [Journal Article]. *Environmental Science Technology*, *43*(4), 1226-1231. Retrieved from `https://doi.org/10.1021/es8018429` doi: 10.1021/es8018429

Aradóttir, E. S. P., Gunnarsson, I., Sigfússon, B., Gunnarsson, G., Júliusson, B. M., Gunnlaugsson, E., ... Sonnenthal, E. (2015). Toward cleaner geothermal energy utilization: Capturing and sequestering co and h2s emissions from geothermal power plants [Journal Article]. *Transport in Porous Media*, *108*(1), 61-84.

Aradóttir, E. S. P., Sonnenthal, E. L., Björnsson, G., & Jónsson, H. (2012). Multidimensional reactive transport modeling of co2 mineral sequestration in basalts at the hellisheidi geothermal field, iceland [Journal Article]. *International Journal of Greenhouse Gas Control*, *9*, 24-40.

Árnason, B., Theódórsson, P., Björnsson, S., & Saemundsson, K. (1969). Hengill, a high temperature thermal area in iceland. *Bulletin volcanologique*, *33*, 245–259.

Arnórsson, S., Gunnlaugsson, E., & Svavarsson, H. (1983). The chemistry of geothermal waters in iceland. ii. mineral equilibria and independent variables controlling water compositions. *Geochimica et Cosmochimica Acta*, *47*(3), 547–566.

Arps, J. J. (1953). The effect of temperature on the density and electrical resistivity of sodium chloride solutions. *Journal of Petroleum Technology*, *5*(10), 17–20.

Bacon, D. H., Ramanathan, R., Schaef, H. T., & McGrail, B. P. (2014). Simulating geologic co-sequestration of carbon dioxide and hydrogen sulfide in a basalt formation. *International Journal of Greenhouse Gas Control*, *21*, 165–176.

Bertin, J., & Loeb, J. (1976). *Experimental and theoretical aspects of induced polarization, vol. 1* (R. G. van Nostrand & S. Saxov, Eds.). Stuttgart, Germany: Schweizerbart Science Publishers. Retrieved from `http://www.schweizerbart.de//publications/detail/isbn/9783443130091/Bertin\_Loeb\_Induced\_Polarization\_Vol`

Binley, A., & Slater, L. (2020). *Resistivity and induced polarization: Theory and applications to the near-surface earth*. Cambridge University Press.

Bochet, O., Bethencourt, L., Dufresne, A., Farasin, J., Pédrot, M., Labasque, T., ... others (2020). Iron-oxidizer hotspots formed by intermittent oxic–anoxic fluid mixing in fractured rocks. *Nature Geoscience*, *13*(2), 149–155.

Börner, J. H., Girault, F., Bhattarai, M., Adhikari, L. B., Deldicque, D., Perrier, F., & Spitzer, K. (2018). Anomalous complex electrical conductivity of a graphitic black schist from the himalayas of central nepal. *Geophysical Research Letters*,

45(9), 3984–3993.

Bücker, M., Flores Orozco, A., & Kemna, A. (2018). Electro-chemical polarization around metallic particles–part 1: The role of diffuse-layer and volume-diffusion relaxation. *Geophysics*, *83*(4), 1–53.

Bücker, M., Flores Orozco, A., & Kemna, A. (2018). Electro-chemical polarization around metallic particles–part 1: The role of diffuse-layer and volume-diffusion relaxation [Journal Article]. *Geophysics*, *83*(4), 1-53.

Carbfix. (2022). *Permanent and secure geological storage of co2 by in-situ carbon mineralization. technical report.* (Report).

Chelidze, T. L., & Gueguen, Y. (1999). Electrical spectroscopy of porous rocks: A review–i. theoretical models. *Geophysical Journal International*, *137*(1), 1–15.

Clark, D. E., Oelkers, E. H., Gunnarsson, I., Sigfússon, B., Snæbjörnsdóttir, S. Ó., Aradottir, E. S., & Gíslason, S. R. (2020). Carbfix2: Co2 and h2s mineralization during 3.5 years of continuous injection into basaltic rocks at more than 250 c. *Geochimica et Cosmochimica Acta*, *279*, 45–66.

Cole, K. S., & Cole, R. H. (1941). Dispersion and absorption in dielectrics. i. alternating current characteristics. [Journal Article]. *J. Chem. Phys.*, *9*, 341-351.

Crovisier, J.-L., Honnorez, J., Fritz, B., & Petit, J.-C. (1992). Dissolution of subglacial volcanic glasses from iceland: laboratory study and modelling. *Applied Geochemistry*, *7*, 55–81.

Cuoco, E., Tedesco, D., Poreda, R. J., Williams, J. C., De Francesco, S., Balagizi, C., & Darrah, T. H. (2013). Impact of volcanic plume emissions on rain water chemistry during the january 2010 nyamuragira eruptive event: implications for essential potable water resources [Journal Article]. *Journal of hazardous materials*, *244*, 570-581.

Daval, D., Sissmann, O., Menguy, N., Saldi, G. D., Guyot, F., Martinez, I., ... Hellmann, R. (2011). Influence of amorphous silica layer formation on the dissolution rate of olivine at 90Ã‚Â°c and elevated pco2 [Journal Article]. *Chemical Geology*, *284*(1-2), 193-209. (00092541)

Davidson, D. W., & Cole, R. H. (1951). Dielectric relaxation in glycerol, propylene glycol, and n-propanol. *The Journal of Chemical Physics*, *19*(12), 1484–1490.

Delmelle, P., Maters, E., & Oppenheimer, C. (2015). Volcanic influences on the carbon, sulfur, and halogen biogeochemical cycles [Book Section]. In *The encyclopedia of volcanoes* (p. 881-893). Elsevier.

Fiandaca, G., Olsson, P.-I., Maurya, P. K., Kühl, A., Bording, T., Dahlin, T., & Auken, E. (2022). Heterodox transients in time-domain-induced polarization. *Geophysics*, *87*(1), E35–E47.

Flaathen, T. K., & Gislason, S. R. (2007). The effect of volcanic eruptions on the chemistry of surface waters: The 1991 and 2000 eruptions of mt. hekla, iceland [Journal Article]. *Journal of Volcanology and Geothermal Research*, *164*(4), 293-316.

Floor, G. H., Calabrese, S., Román-Ross, G., & Aiuppa, A. (2011). Selenium mobilization in soils due to volcanic derived acid rain: an example from mt etna volcano, sicily [Journal Article]. *Chemical Geology*, *289*(3-4), 235-244.

Flores Orozco, A., Velimirovic, M., Tosco, T., Kemna, A., Sapion, H., Klaas, N., ... Bastiaens, L. (2015). Monitoring the injection of microscale zerovalent iron particles for groundwater remediation by means of complex electrical conductivity imaging. *Environmental Science & Technology*, *49*(9), 5593–5600.

Flores Orozco, A., Williams, K. H., Long, P. E., Hubbard, S. S., & Kemna, A. (2011). Using complex resistivity imaging to infer biogeochemical processes associated with bioremediation of an uranium-contaminated aquifer. *Journal of Geophysical Research: Biogeosciences*, *116*(G3).

Flóvenz, O. G., Spangenberg, E., Kulenkampf, J., Árnason, K., Karlsdóttir, R., & Huenges, E. (2005). The role of electrical interface conduction in geothermal exploration [Conference Proceedings]. In *Proceedings of world geothermal*

congress 2005.

Foulger, G. R. (1988). Hengill triple junction, sw iceland 1. tectonic structure and the spatial and temporal distribution of local earthquakes. *Journal of Geophysical Research: Solid Earth*, *93*(B11), 13493-13506. Retrieved from `https://agupubs.onlinelibrary.wiley.com/doi/abs/10.1029/JB093iB11p13493` doi: https://doi.org/10.1029/JB093iB11p13493

Foulger, G. R., & Toomey, D. R. (1989). Structure and evolution of the hengill-grensdalur volcanic complex, iceland: Geology, geophysics, and seismic tomography. *Journal of Geophysical Research: Solid Earth*, *94*(B12), 17511–17522.

Franzson, H. (1988). *Nesjavellir-borholujarðfræði, vatnsgengd í jarðhitageymi* (Technical report No. OS-88046/JHD-09). Orkustofnun.

Franzson, H., & Gunnlaugsson, E. (2020). Formation of clays and chlorites in the upper icelandic crust. In *Proceedings world geothermal congress.*

Fridriksson, T., Mateos, A., Audinet, P., & Orucu, Y. (2016). Greenhouse gases from geothermal power production [Journal Article].

Galeczka, I., Sigurdsson, G., Eiriksdottir, E. S., Oelkers, E. H., & Gislason, S. R. (2016). The chemical composition of rivers and snow affected by the 2014/2015 bárðarbunga eruption, iceland [Journal Article]. *Journal of Volcanology and Geothermal Research*, *316*, 101-119.

Galeczka, I., Stefánsson, A., Kleine, B. I., Gunnarsson-Robin, J., Snæbjörnsdóttir, S. o., Sigfússon, B., ... Oelkers, E. H. (2022). A pre-injection assessment of co2 and h2s mineralization reactions at the nesjavellir (iceland) geothermal storage site [Journal Article]. *International Journal of Greenhouse Gas Control*, *115*, 103610.

Gómez-Díaz, E., Scott, S., Ratouis, T., & Newson, J. (2022). Numerical modeling of reinjection and tracer transport in a shallow aquifer, nesjavellir geothermal system, iceland [Journal Article]. *Geothermal Energy*, *10*(1), 1-28.

Greaver, T. L., Sullivan, T. J., Herrick, J. D., Barber, M. C., Baron, J. S., Cosby, B. J., ... Goodale, C. L. (2012). Ecological effects of nitrogen and sulfur air pollution in the us: what do we know? [Journal Article]. *Frontiers in Ecology and the Environment*, *10*(7), 365-372.

Gudmundsson, A., Mortensen, A. K., Hjartarson, A., Karlsdóttir, R., & Ármannsson, H. (2010). Exploration and utilization of the Namafjall high temperature area in North Iceland [Conference Proceedings]. In *Proceedings of world geothermal congress 2010.*

Gunnarsdottir, S. H., Helgadottir, H. M., & Snaebjornsdottir, S. (2020). Geco: Geological properties, permeability and porosity of the nesjavellir high temperature area in relation to the re-injection of geothermal co2 and h2s gases. In *Proceedings world geothermal congress.*

Gunnarsson, I., Aradóttir, E. S., Oelkers, E. H., Clark, D. E., Arnarson, M. , Sigfússon, B., ... Júlíusson, B. M. (2018). The rapid and cost-effective capture and subsurface mineral storage of carbon and sulfur at the carbfix2 site [Journal Article]. *International Journal of Greenhouse Gas Control*, *79*, 117-126.

Gunnlaugsson, E., & Arnòrsson, S. (1982). The chemistry of iron in geothermal systems in iceland. *Journal of Volcanology and Geothermal Research*, *14*(3-4), 281–299.

Gurin, G., Titov, K., & Ilyin, Y. (2019). Induced polarization of rocks containing metallic particles: evidence of passivation effect. *Geophysical Research Letters*, *46*(2), 670–677.

Gurin, G., Titov, K., Ilyin, Y., & Tarasov, A. (2015). Induced polarization of disseminated electronically conductive minerals: a semi-empirical model. *Geophysical Journal International*, *200*(3), 1555–1565.

Gysi, A. P., & Stefánsson, A. (2008). Numerical modelling of co2-water-basalt interaction [Journal Article]. *Mineralogical Magazine*, *72*(1), 55-59.

Hafstað, T. H. (2003). *Niðurrennslisholurnar nn-3 og nn-4 á nesjavöllum* (Field re-

port in Icelandic No. ThHH-03-06). ISOR.

Halisch, M., Hupfer, S., Weller, A., Dlugosch, R., & Plumhoff, H.-P. (2018). An experimental setup for the assessment of effects of carbonate rock dissolution on complex electrical conductivity spectra. In *Paper sca2018-051 international symposium of the society of core analysts held in trondheim, norway* (pp. 27–31).

Havriliak, S., & Negami, S. (1966). A complex plane analysis of α-dispersions in some polymer systems. In *Journal of polymer science: Polymer symposia* (Vol. 14, pp. 99–117).

Helander, D. P. (1983). *Fundamentals of formation evaluation* (OGCI Publications, Tulsa, Oklahoma, Ed.). Oil & Gas Consultants Intl. Retrieved from `https://openlibrary.org/books/OL3510096M/Fundamentals_of_formation_evaluation` (ISBN: 978-0930972028)

Helgadóttir, H. M. (2021). *Nn-03 and nn-04 in nesjavellir drill cuttings analysis.* (Technical report). ISOR.

Hermans, T., Goderniaux, P., Jougnot, D., Fleckenstein, J. H., Brunner, P., Nguyen, F., ... Lopez Alvis, J. (2023). Advancing measurements and representations of subsurface heterogeneity and dynamic processes: towards 4d hydrogeology [Journal Article]. *Hydrology and Earth System Sciences*, *27*(1), 255-287.

Iceland Ministry of the Environment, Energy and Climate. (2010). *Regulation no. 514/2010* (Tech. Rep.).

Izumoto, S., Huisman, J. A., Wu, Y., & Vereecken, H. (2020). Effect of solute concentration on the spectral induced polarization response of calcite precipitation [Journal Article]. *Geophysical journal international*, *220*(2), 1187-1196.

Kristinsdóttir, L. H., Flóvenz, o. G., Árnason, K., Bruhn, D., Milsch, H., Spangenberg, E., & Kulenkampff, J. (2010). Electrical conductivity and p-wave velocity in rock samples from high-temperature icelandic geothermal fields [Journal Article]. *Geothermics*, *39*(1), 94-105. (03756505)

Larsen, J. J., Lévy, L., & Asif, M. R. (2022). Removal of powerline noise in geophysical datasets with a scientific machine-learning based approach [Journal Article]. *IEEE Transactions on Geoscience and Remote Sensing*, *60*, 1-10. doi: 10.1109/TGRS.2022.3223737

Lévy, L. (2019). *Electrical properties of hydrothermally altered rocks: observations and interpretations based on laboratory, field and borehole studies at Krafla volcano, Iceland* (Doctoral dissertation, Ecole Normale Supérieure and University of Iceland). Retrieved from `https://hdl.handle.net/20.500.11815/1140`

Lévy, L., Gibert, B., Escobedo, D., Patrier, P., Lanson, B., Beaufort, D., ... Marino, N. (2020). Relationships between lithology, permeability, clay mineralogy and electrical conductivity in icelandic altered volcanic rocks. In *Proceedings world geothermal congress* (Vol. 1).

Lévy, L., Gibert, B., Sigmundsson, F., Flóvenz, O. G., Hersir, G. P., Briole, P., & Pezard, P. A. (2018). The role of smectites in the electrical conductivity of active hydrothermal systems: electrical properties of core samples from Krafla volcano, Iceland. *Geophysical Journal International*, *215*(3), 1558-1582.

Lévy, L., Gibert, B., Sigmundsson, F., Parat, F., Deldicque, D., & Hersir, G. P. (2019, March). Tracking magmatic hydrogen sulphur circulations using electrical impedance : complex electrical properties of core samples at the Krafla volcano, Iceland. *Journal of Geophysical Research: Solid Earth*, *124*(3), 2492–2509. doi: https://doi.org/10.1029/2018JB016814

Lévy, L., Maurya, P., Byrdina, S., Vandemeulebrouck, J., Sigmundsson, F., Arnason, K., & al., e. (2019). Electrical resistivity tomography and time-domain induced polarization field investigations of geothermal areas at krafla, iceland: comparison to borehole and laboratory frequency-domain electrical observations [Journal Article]. *Geophysical Journal International*.

Lévy, L., Thalund-Hansen, R., Bording, T., Fiandaca, G., Christiansen, A. V., Rügge, K., ... Bjerg, P. L. (2022). Quantifying reagent spreading by cross-borehole electrical tomography to assess performance of groundwater remediation [Journal Article]. *Water Resources Research*, *58*(9), e2022WR032218. Retrieved from https://doi.org/10.1029/2022WR032218 (https://doi.org/10.1029/2022WR032218) doi: https://doi.org/10.1029/2022WR032218

Lévy, L., Weller, A., & Gibert, B. (2019). Influence of smectite and salinity on the imaginary and surface conductivity of volcanic rocks [Journal Article]. *Near Surface Geophysics*, *17*(6-Recent Developments in Induced Polarization), 653-673.

Lévy, L. (2023). *Geophysical monitoring data GEMGAS [Dataset].* https://doi.org/10.5281/zenodo.10145643. Zenodo.

Mamrosh, D. L., McIntush, K. E., Douglas, A., Fisher, K. S., Júlíusson, B. M., Gunnarsson, I., ... Arnarson, M. (2014). Removal of hydrogen sulfide and recovery of carbon dioxide from geothermal non-condensable gas using water [Journal Article]. *Transactions - Geothermal Resources Council*(38).

Mao, D., Revil, A., & Hinton, J. (2016). Induced polarization response of porous media with metallic particles—part 4: Detection of metallic and nonmetallic targets in time-domain-induced polarization tomography [Journal Article]. *Geophysics*, *81*(4), D359-D375.

Marieni, C., Přikryl, J., Aradóttir, E. S., Gunnarsson, I., & Stefánsson, A. (2018). Towards 'green'geothermal energy: Co-mineralization of carbon and sulfur in geothermal reservoirs [Journal Article]. *International Journal of Greenhouse Gas Control*, *77*, 96-105.

Martin, T., Titov, K., Tarasov, A., & Weller, A. (2021). Spectral induced polarization: frequency domain versus time domain laboratory data [Journal Article]. *Geophysical Journal International*, *225*(3), 1982-2000.

Martin, T., & Weller, A. (2023). Superposition of induced polarization signals measured on pyrite–sand mixtures [Journal Article]. *Geophysical Journal International*, *234*(1), 699-711. Retrieved from https://doi.org/10.1093/gji/ggad091 doi: 10.1093/gji/ggad091

Matter, J. M., Stute, M., Snæbjörnsdottir, S. o., Oelkers, E. H., Gislason, S. R., Aradottir, E. S., ... Gunnlaugsson, E. (2016). Rapid carbon mineralization for permanent disposal of anthropogenic carbon dioxide emissions [Journal Article]. *Science*, *352*(6291), 1312-1314.

Mellage, A., Holmes, A. B., Linley, S., Vallee, L., Rezanezhad, F., Thomson, N., ... Van Cappellen, P. (2018). Sensing coated iron-oxide nanoparticles with spectral induced polarization (sip): experiments in natural sand packed flow-through columns [Journal Article]. *Environmental science technology*, *52*(24), 14256-14265.

Mendieta, A., Jougnot, D., Leroy, P., & Maineult, A. (2021). Spectral induced polarization characterization of non-consolidated clays for varying salinities—an experimental study [Journal Article]. *Journal of Geophysical Research: Solid Earth*, *126*(4), e2020JB021125.

Menefee, A. H., Giammar, D. E., & Ellis, B. R. (2018). Permanent co2 trapping through localized and chemical gradient-driven basalt carbonation [Journal Article]. *Environmental science technology*, *52*(15), 8954-8964. Retrieved from https://doi.org/10.1021/acs.est.8b01814 doi: 10.1021/acs.est.8b01814

Mielke, R. E., Pace, D. L., Porter, T., & Southam, G. (2003). A critical stage in the formation of acid mine drainage: Colonization of pyrite by acidithiobacillus ferrooxidans under ph-neutral conditions. *Geobiology*, *1*(1), 81–90.

Mount Sopris QL40-FTC. (2014). https://mountsopris.com/ql40-ftc-fluid-conductivity-and-temperature/. (Accessed: 2023-11-06)

Mount Sopris QL40-IP. (2020). https://mountsopris.com/ql40-ip-induced-polarization/. (Accessed: 2023-11-06)

Nordsiek, S., & Weller, A. (2008). A new approach to fitting induced-polarization spectra. *Geophysics*, *73*(6), F235–F245.

Olhoeft, G. R. (1985). Low-frequency electrical properties. *Geophysics*, *50*(12), 2492-2503.

Olsson, P.-I., Fiandaca, G., Larsen, J. J., Dahlin, T., & Auken, E. (2016, November). Doubling the spectrum of time-domain induced polarization by harmonic de-noising, drift correction, spike removal, tapered gating and data uncertainty estimation. *Geophysical Journal International*, *207*(2), 774–784. (DOI: https://doi.org/10.1093/gji/ggw260)

Pelton, W. H., Sill, W. R., & Smith, B. D. (1983). Interpretation of complex resistivity and dielectric data. part i [Journal Article]. *Geophysical Transactions*, *29*(4), 297-330.

Pelton, W. H., Ward, S. H., Hallof, P. G., Sill, W. R., & Nelson, P. H. (1978). Mineral discrimination and removal of inductive coupling with multifrequency IP. *Geophysics*, *43*(3), 588-609.

Percak-Dennett, E., He, S., Converse, B., Konishi, H., Xu, H., Corcoran, A., ... others (2017). Microbial acceleration of aerobic pyrite oxidation at circumneutral ph. *Geobiology*, *15*(5), 690–703.

Peshtani, K., Weller, A., Saneiyan, S., & Slater, L. (2022). The influence of magnetic minerals on induced polarization measurements in sedimentary rocks. *Geophysical Research Letters*, *49*(19), e2022GL100192.

Placencia-Gómez, E. (2015). *Spectral induced polarization investigations in presence of metal sulphide minerals: implications for monitoring the generation of acid mine drainage* (Doctoral dissertation, Aalto University - Department of Civil and Environmental Engineering). Retrieved from https://aaltodoc.aalto.fi/handle/123456789/17577

Placencia-Gómez, E., Slater, L., Ntarlagiannis, D., & Binley, A. (2013). Laboratory sip signatures associated with oxidation of disseminated metal sulfides. *Journal of Contaminant Hydrology*, *148*, 25–38.

Plummer, L. N., Parkhurst, D. L., & Wigley, T. M. L. (1979). Critical review of the kinetics of calcite dissolution and precipitation [Journal Article].

Pridmore, D. F., & Shuey, R. T. (1976). The electrical resistivity of galena, pyrite, and chalcopyrite [Journal Article]. *American Mineralogist*, *61*(3-4), 248-259.

Prikryl, J., Marieni, C., Gudbrandsson, S., Aradóttir, E. S., Gunnarsson, I., & Stefánsson, A. (2018). H 2 s sequestration process and sustainability in geothermal systems. *Geothermics*, *71*, 156–166.

Ratouis, T. M. P., Snæbjörnsdóttir, S. o., Voigt, M. J., Sigfússon, B., Gunnarsson, G., Aradóttir, E. S., & Hjörleifsdóttir, V. (2022). Carbfix 2: A transport model of long-term co2 and h2s injection into basaltic rocks at hellisheidi, sw-iceland [Journal Article]. *International Journal of Greenhouse Gas Control*, *114*, 103586.

Rembert, F. (2021). Development of geo-electrical methods to characterize dissolution and precipitation processes in a carbonate context [Journal Article].

Revil, A., Abdel Aal, G. Z., Atekwana, E. A., Mao, D., & Florsch, N. (2015). Induced polarization response of porous media with metallic particles - Part 2: comparison with a broad database of experimental data [Journal Article]. *Geophysics*, *80*(5), D539-D552.

Revil, A., Coperey, A., Mao, D., Abdulsamad, F., Ghorbani, A., Rossi, M., & Gasquet, D. (2018). Induced polarization response of porous media with metallic particles—part 8: Influence of temperature and salinity. *Geophysics*, *83*(6), E435–E456.

Revil, A., Florsch, N., & Mao, D. (2015). Induced polarization response of porous media with metallic particles - Part 1: a theory for disseminated semiconduc-

tors [Journal Article]. *Geophysics*, *80*(5), 525–538.

Revil, A., Hermitte, D., Spangenberg, E., & CochemÃfÂ©, J. J. (2002). Electrical properties of zeolitized volcaniclastic material [Journal Article]. *Journal of Geophysical Research*, *107*.

Revil, A., Sleevi, M. F., & Mao, D. (2017). Induced polarization response of porous media with metallic particles–part 5: Influence of the background polarization. *Geophysics*, *82*(2), E77–E96.

Robin, J. G., Stefansson, A., Ono, S., Gunnarsson, I., & Aradóttir, E. S. (2020). H2s sequestration traced by sulfur isotopes at hellisheiði geothermal system, iceland. *Geothermics*, *83*, 101730.

Roy, A., & Dhar, R. (1971). Radius of investigation in dc resistivity well logging. *Geophysics*, *36*(4), 754–760.

Saneiyan, S., Ntarlagiannis, D., Werkema Jr, D. D., & Ustra, A. (2018). Geophysical methods for monitoring soil stabilization processes [Journal Article]. *Journal of applied geophysics*, *148*, 234-244.

Schiffman, P., & Fridleifsson, G. (1991). The smectite-chlorite transition in drillhole n 1-15, nesjavellir geothermal field, iceland : Xrd, bse and electron microprobe investigations [Journal Article]. *Journal of Metamorphic Geology*, *9*, 679-696.

Shuey, R. T. (2012). *Semiconducting ore minerals* (Vol. 4) [Book]. Elsevier.

Slater, L., Choi, J., & Wu, Y. (2005). Electrical properties of iron-sand columns: Implications for induced polarization investigation and performance monitoring of iron-wall barriers [Journal Article]. *Geophysics*, *70*(4), G87-G94.

Slater, L., Ntarlagiannis, D., Personna, Y. R., & Hubbard, S. (2007). Pore-scale spectral induced polarization signatures associated with fes biomineral transformations. *Geophysical Research Letters*, *34*(21).

Slater, L., Ntarlagiannis, D., & Wishart, D. (2006). On the relationship between induced polarization and surface area in metal-sand and clay-sand mixtures [Journal Article]. *Geophysics*, *71*(2), A1-A5.

Snæbjörnsdóttir, S. Ó., Galeczka, I., Sigfússon, B., & Oelkers, E. H. (2020). Injection of geothermal co2 and h2s gases at the nesjavellir site, sw iceland: A pre-injection overview. In *Proceedings of the world geothermal congress, april 26-may 2, reykjavik, iceland* (Vol. 6).

Stefánsson, A., Arnórsson, S., Gunnarsson, I., Kaasalainen, H., & Gunnlaugsson, E. (2011). The geochemistry and sequestration of H2S into the geothermal system at Hellisheidi, Iceland. *Journal of Volcanology and Geothermal Research*, *202*(3-4), 179–188.

Stefánsson, A., & Gíslason, S. R. (2001). Chemical weathering of basalts, southwest iceland: effect of rock crystallinity and secondary minerals on chemical fluxes to the ocean. *American Journal of Science*, *301*(6), 513–556.

Strobel, C., Abramov, S., Huisman, J., Cirpka, O., & Mellage, A. (2023). Spectral induced polarization (sip) of denitrification-driven microbial activity in column experiments packed with calcareous aquifer sediments. *Journal of Geophysical Research: Biogeosciences*, *128*(1), e2022JG007190.

Sumner, J. S. (1976). Principles of induced polarization for geophysical exploration. In *Developments in economic geology, 5.* Elsevier Scientific Publishing Company Amsterdam.

Tarasov, A., & Titov, K. (2007). Relaxation time distribution from time domain induced polarization measurements. *Geophysical Journal International*, *170*(1), 31–43.

Tarasov, A., & Titov, K. (2013). On the use of the cole–cole equations in spectral induced polarization [Journal Article]. *Geophysical Journal International*, *195*(1), 352-356.

Telford, W. M., Geldart, L. P., & Sheriff, R. E. (1990). *Applied Geophysics* (2nd ed.). Cambridge University Press. doi: 10.1017/CBO9781139167932

Trias, R., Ménez, B., le Campion, P., Zivanovic, Y., Lecourt, L., Lecoeuvre, A., ... others (2017). High reactivity of deep biota under anthropogenic co2 injection into basalt. *Nature communications*, *8*(1), 1063.

Wang, J., Ryan, D., Anthony, E. J., Wildgust, N., & Aiken, T. (2011). Effects of impurities on co2 transport, injection and storage [Journal Article]. *Energy Procedia*, *4*, 3071-3078. Retrieved from `https://www.sciencedirect.com/science/article/pii/S1876610211004164` doi: https://doi.org/10.1016/j.egypro.2011.02.219

Waxman, M. H., & Smits, L. J. M. (1968). Electrical conductivities in oil-bearing shaly sands [Journal Article]. *Soc. Pet. Eng. J.*, *8*, 107-122.

Weller, A., & Slater, L. (2022). Ambiguity in induced polarization time constants and the advantage of the pelton model. *Geophysics*, *87*(6), E393–E399.

White, S. K., Spane, F. A., Schaef, H. T., Miller, Q. R. S., White, M. D., Horner, J. A., & McGrail, B. P. (2020). Quantification of co2 mineralization at the wallula basalt pilot project [Journal Article]. *Environmental Science Technology*, *54*(22), 14609-14616. Retrieved from `https://doi.org/10.1021/acs.est.0c05142` doi: 10.1021/acs.est.0c05142

Williams, K. H., Ntarlagiannis, D., Slater, L. D., Dohnalkova, A., Hubbard, S. S., & Banfield, J. F. (2005). Geophysical imaging of stimulated microbial biomineralization. *Environmental science & technology*, *39*(19), 7592–7600.

Williamson, M. A., & Rimstidt, J. D. (1994). The kinetics and electrochemical rate-determining step of aqueous pyrite oxidation [Journal Article]. *Geochimica et Cosmochimica Acta*, *58*(24), 5443-5454.

World Health Organization - Regional Office for Europe. (2000). *Air quality guidelines for europe* (Tech. Rep.). `https://iris.who.int/bitstream/handle/10665/107335/9789289013581-eng.pdf?sequence=1`.

Wu, Y., Ajo-Franklin, J. B., Spycher, N., Hubbard, S. S., Zhang, G., Williams, K. H., ... Smith, R. (2011). Geophysical monitoring and reactive transport modeling of ureolytically-driven calcium carbonate precipitation [Journal Article]. *Geochemical transactions*, *12*(1), 1-20.

Wu, Y., Hubbard, S., Williams, K. H., & Ajo-Franklin, J. (2010). On the complex conductivity signatures of calcite precipitation [Journal Article]. *Journal of Geophysical Research: Biogeosciences*, *115*(G2).

Zakharova, O. K., & Spichak, V. V. (2012). Geothermal fields of hengill volcano, iceland [Journal Article]. *Journal of Volcanology and Seismology*, *6*(1), 1-14.

Zhang, C., Slater, L., Redden, G., Fujita, Y., Johnson, T., & Fox, D. (2012). Spectral induced polarization signatures of hydroxide adsorption and mineral precipitation in porous media [Journal Article]. *Environmental science technology*, *46*(8), 4357-4364.

Appendix A Added-value and justification of the stretched exponential fitting procedure

The stretched exponential function $f(t) = \alpha e^{-(\frac{t}{\tau_{KWW}})^{\beta}}$, also named Kohlrausch-Williams-Watts (KWW), and the Havriliak-Negami (HN) relaxation function $g(\omega) = \frac{1}{(1+(i\omega\tau_{HN})^{\alpha}_{HN})^{\gamma}_{HN}}$ have been widely used to describe the relaxation behavior of glass-forming liquids and complex systems, in time- and frequency-domain respectively (Alvarez et al., 1991). The HN relaxation function is a generalization of the Pelton model with one more parameter (Havriliak & Negami, 1966). It also corresponds to the "Generalized Cole-Cole" model (Pelton et al., 1983). A relationship among the parameters of the KWW and HN models is suggested by the fact that both models yield an accurate description of real data. An empirical and mathematical relation between the coefficients of the KWW and HN functions is found by Alvarez et al. (1991). This relationship is not analytical since the HN and the KWW relaxation functions are not exactly Fourier transforms of

each other. In particular, the relation between the relaxation times in both functions depends on the exponent beta in the KWW function, β. For example, for β close to 1, $\tau_{HN} \simeq \tau_{KWW}$, and for $\beta = 0.1$, $\tau_{HN} = 300\tau_{KWW}$. The KWW has one less parameter, so it can always be transformed into an HN model, but the contrary is not always true. The product $\alpha_{HN}\gamma_{HN}$ is close to β. In addition, even though the HN model is a generalized version of the Pelton model, the fitted chargeability parameter cannot be used to quantify pyrite as it is not strictly comparable to the chargeability in the Pelton model.

That's why the Debye decomposition is used here to relate the measured TDIP data with petrophysical relationships calibrated on FDIP data.

Nevertheless, based on the theory described by Alvarez et al. (1991), the stretched exponential function is used to automatically discriminate noisy discharge curves that do not follow the stretched exponential shape. Debye decomposition is only applied to discharge curves that can be reasonably fitted by a stretched exponential. Moreover, the stretched exponential fit allows smoothing out the "accepted" discharge curves that may still contain some noise, which in turn results in more meaningful outcomes from the Debye decomposition. This is illustrated for the total chargeability, M_{tot}, and the mean relaxation time, τ_{mean} in Figures A1 and A2. In these figures, Debye decomposition carried out on the stretched exponential fitted function is compared to Debye decomposition carried out on the polarizability data themselves (before the fitting step). The comparison clearly indicates less noise in the curves of SE fitted spectra.

Appendix B Temperature and borehole diameter in NN3 and NN4

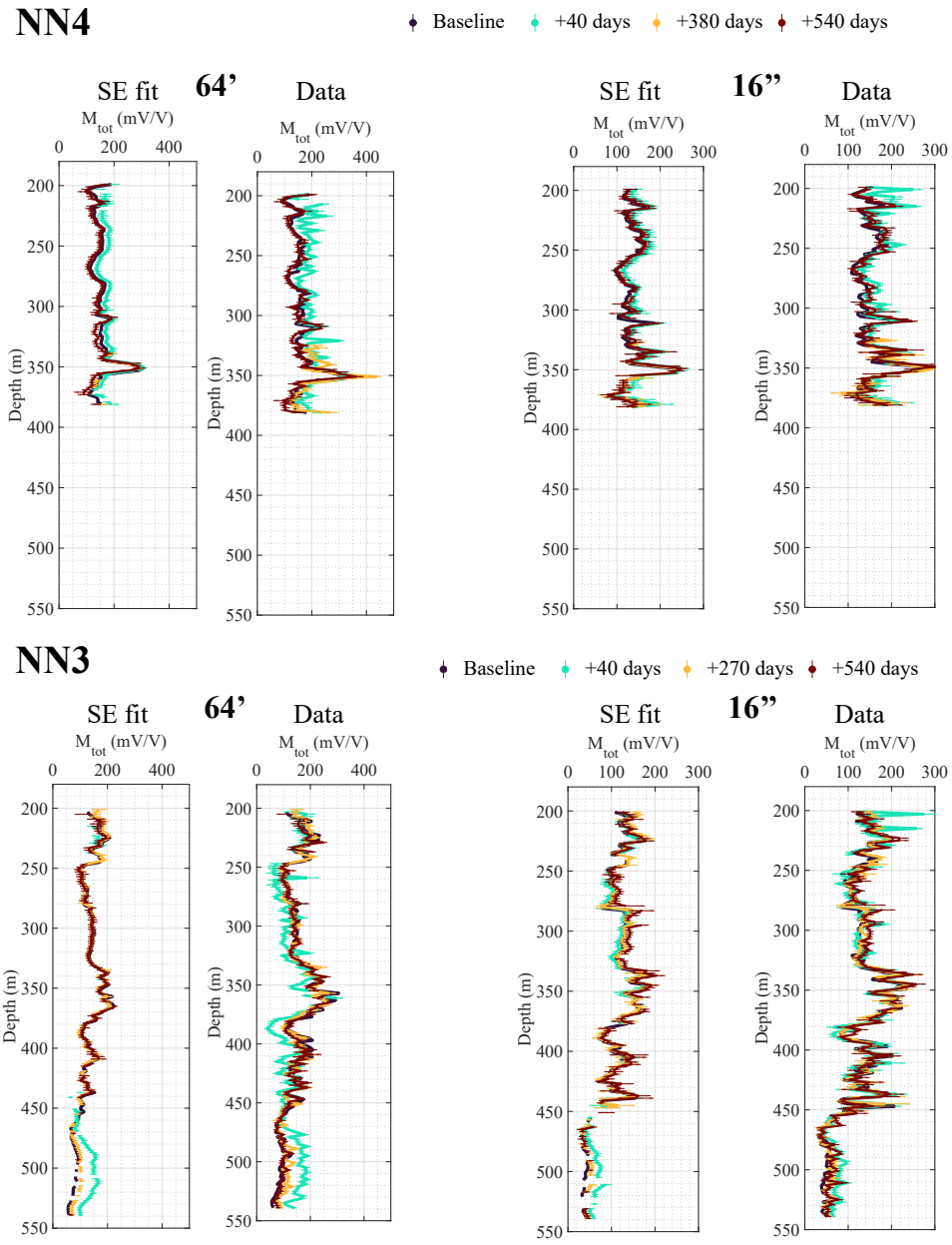

Figure A1. Total chargeability from Debye decomposition in NN3 (top) and NN4 (bottom), with 64" (left) and 16" (right) spacing. The results are shown for Debye decompositions carried out on stretched exponential fit ("SE fit") and on original data. Note that the Debye decomposition on original data includes more discharge curves since it happens before the filtering procedure related to the SE fit.

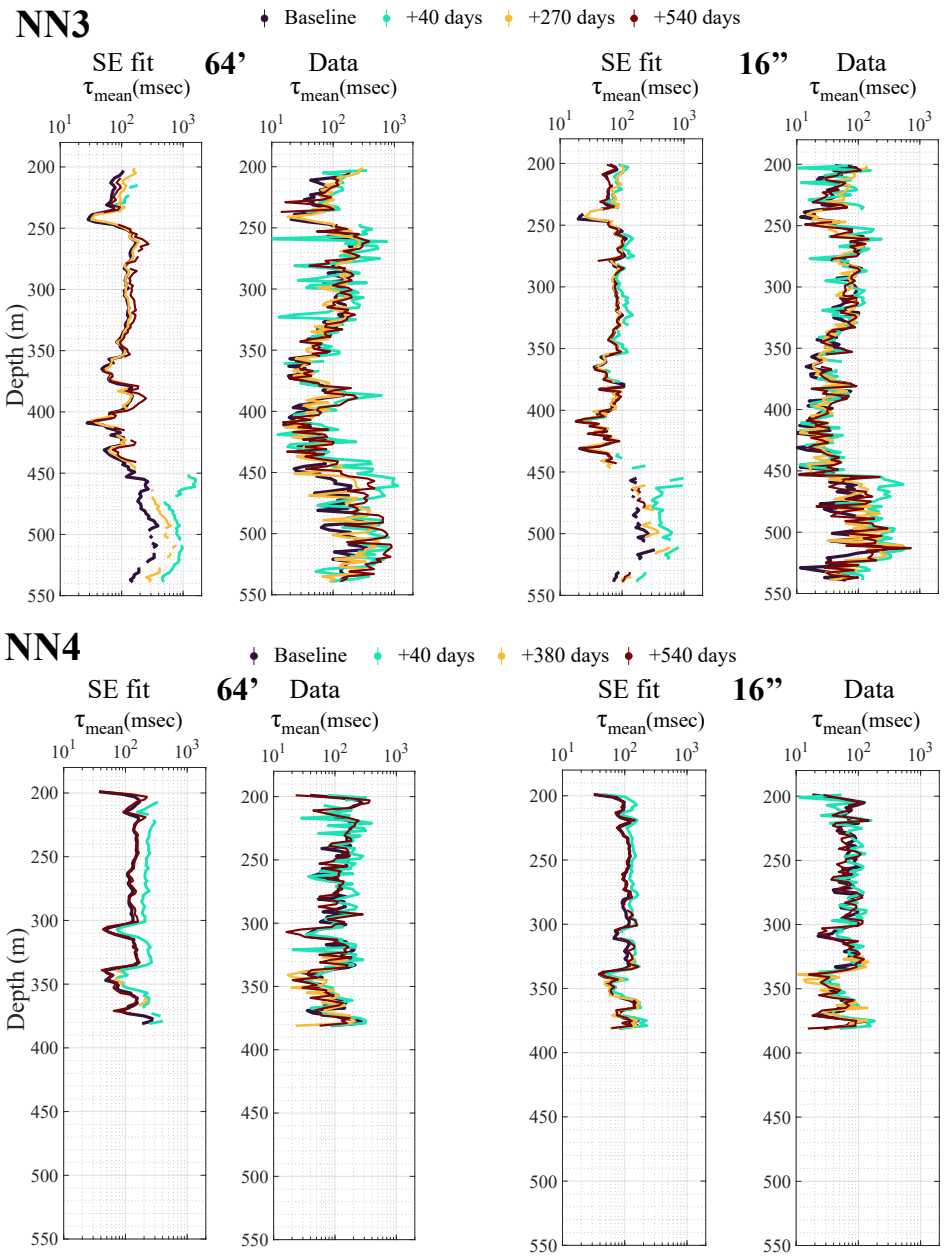

Figure A2. Weighted-average relaxation time from Debye decomposition in NN3 (top) and NN4 (bottom), with 64" (left) and 16" (right) spacing. The results are shown for Debye decompositions carried out on stretched exponential fit ("SE fit") and on original data. Note that the Debye decomposition on original data includes more discharge curves since it happens before the filtering procedure related to the SE fit.

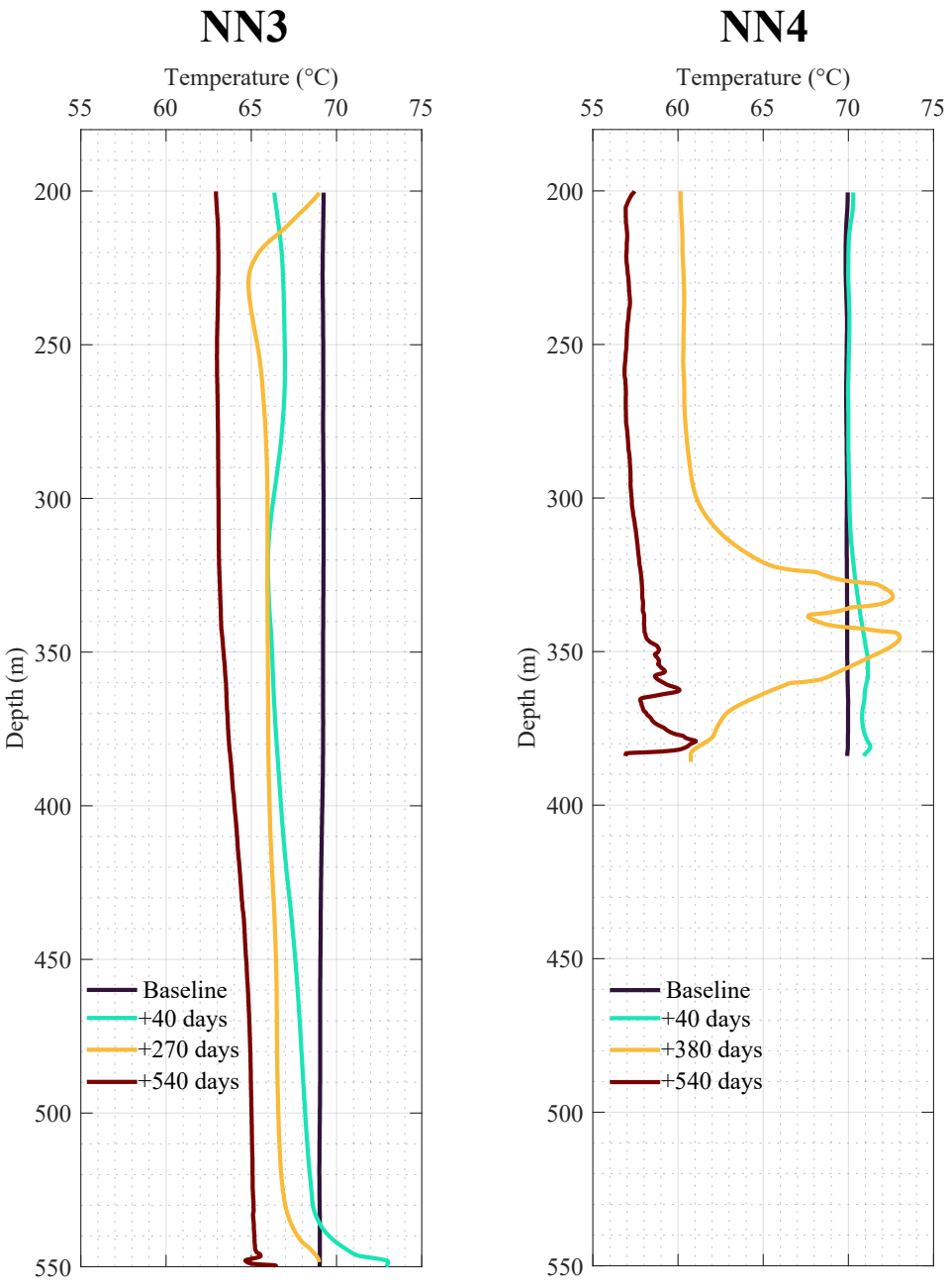

Figure B1. Temperature measured in NN3 and NN4 at the four monitoring rounds.

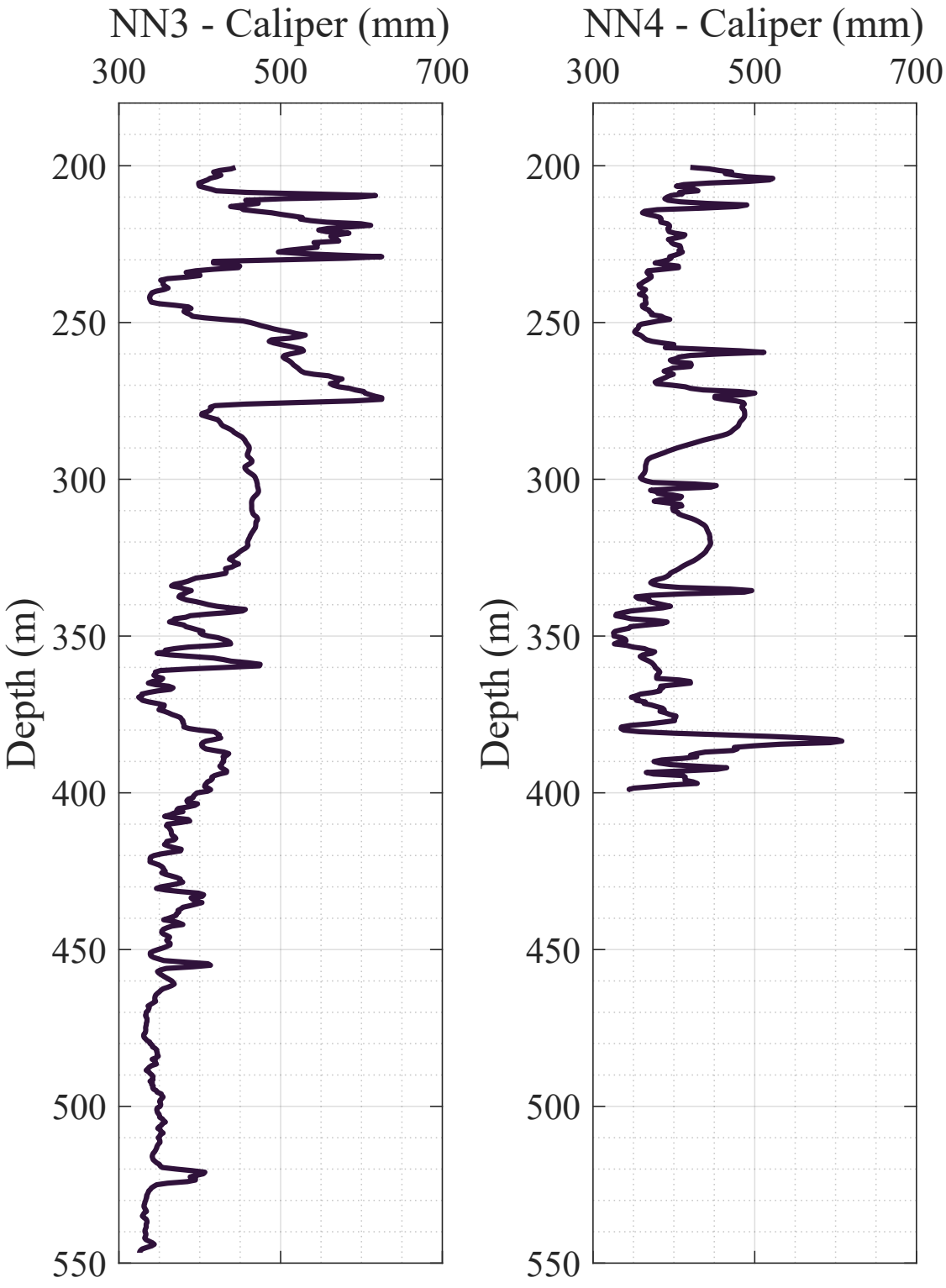

Figure B2. Borehole diameter (caliper) below the casing, measured in 2001 after drilling, in NN3 and NN4.